The tungsten-gold veins of Bonnac (French Massif central): new constraints for a Variscan granite-related genesis

Florent Cheval-Garabédian, Michel Faure, Eric Marcoux, Marc Poujol

The tungsten-gold veins of Bonnac (French Massif central): new constraints for a Variscan granite-related genesis

Les filons à tungstène-or de Bonnac (Massif central français) : nouvelles contraintes pour une genèse reliée aux granites varisques

Florent Cheval-Garabédian[1-2*], Michel Faure[1], Eric Marcoux[1], Marc Poujol[3]

1: Institut des Sciences de la Terre d'Orléans (ISTO), UMR 7327-CNRS/Université d'Orléans/BRGM, 1A Rue de la Férollerie 45071 Orléans Cedex 2, France

2: Present address: Société Minière Georges Montagnat, 30 route de la Baie des Dames, 98800 Nouméa, Nouvelle-Calédonie

3: Université Rennes, CNRS, Géosciences Rennes – UMR 6118, F-35000 Rennes, France

* Corresponding author: florent-cg@hotmail.fr

Published by EDP Sciences and available at https://www.bsgf.fr or https://doi.org/10.1051/bsgf/2020041

Abstract

In the Brioude-Massiac district (French Massif Central: FMC), a network of W-As-Bi-Au quartz veins constitutes the Bonnac deposit, where tungsten is the major economic element, together with high-grade gold (up to 15 g/t Au). The evolution of this mineralization has been divided into 3 stages: i) an early deep-seated wolframite-löllingite stage formed between 12 to 9 km, at up to 400°C, ii) a ductile/brittle deformation stage associated with scheelite and arsenopyrite deposition, with an estimated temperature of 480-300 °C; iii) a late stage controlled by fluid-overpressure potentially triggered by fault-valve mechanism, at a depth of 7 to 5 Km, and a temperature estimated between 266 to 240 °C, is marked by micro-fracturing infilled by native bismuth, bismuthinite, hedleyite, electrum, pyrite and base-metals. Structural analysis, and apatite LA-ICP-MS U/Pb dating, demonstrate a spatial and temporal link between the emplacement of the peraluminous leucogranitic dykes and the Bonnac mineralization. In more details, the mineralization was deposited between 321-316 Ma, during, or just after, the emplacement of the peraluminous dykes estimated around 329-315 Ma, suggesting a magmatic-hydrothermal transition for the ore-forming process. In the proposed model, the cooling of a hidden two-mica granitic pluton could have generated a magmatic fluid, and acted as the heat source responsible for fluid flow towards inherited permeability zones. The magmatic fluid could have then re-equilibrated at high temperature by fluid-rocks interaction. The sharp changes in pressure, associated with the decrease of the temperature, and sulfide-fugacity generated by a late input of meteoric fluid were responsible for the deposition of the late gold-stage. At the regional scale, the tungsten-gold event is ascribed to an early hydrothermal stage, dissociated from the formation of the antimony event in the district. The leucogranitic dykes and Bonnac quartz veins are controlled by a NW-SE stretching direction, interpreted as an expression of the Serpukhovian-Bashkirian syn-orogenic extension (D4 event of the FMC). These new data provide evidence for an early tungsten and gold metallogenic event in the FMC,

prior the “Or300” event. The genetic classification of the Bonnac mineralization is equivocal. The W-As-Bi-Au-quartz veins exhibit the features of both an “orogenic gold” deposit at a relatively deep emplacement level (mesozonal), and an Intrusion-Related-Gold-Deposit (IRGD) type with a spatial-temporal link with the peraluminous intrusion emplacement. We propose that the Bonnac deposits represent an intermediate type between a typical orogenic-gold deposit and an IRGD. We argue that the presence of economic high-grade gold content in tungsten vein-type, and more generally the IRGD deposits, have been underestimated in the Variscan French Massif Central.

Keywords. Tungsten-Gold ore deposit, French Massif Central, IRGD, Variscan metallogeny, Brioude-Massiac district, Apatite U-Pb dating.

Résumé

Dans le district de Brioude-Massiac (Massif Central Français ; FMC), les gîtes de Bonnac correspondent à un réseau de veines de quartz à W-As-Bi-Au. Le tungstène y est le principal métal économique, et est associé à de fortes teneurs en or (entre 1 et 15 g / t Au). L'évolution de cette minéralisation peut être divisée en 3 étapes: i) un stade précoce à wolframite et löllingite, formé en profondeur, entre 12 et 9 km, et à des températures supérieures à 400 °C, ii) un stade de déformation ductile / cassant qui contrôle le dépôt de scheelite et d'arsénopyrite, estimé entre 480-300 °C; iii) un stade tardif, contrôlé par des surpressions de fluide marquées par une micro-fracturation colmatée par une paragenèse à bismuth natif, bismuthinite, hedleyite, électrum, pyrite associée à des métaux de base. Les surpressions de fluide seraient possiblement

provoquées par un mécanisme de valve-sismique, à des températures comprises entre 266 et 240 ° C, à une profondeur estimée entre 7 et < 5 km. L'analyse structurale, et les datations U/Pb sur apatite par la méthode LA-ICP-MS démontrent un lien spatial et temporel entre les dykes leucogranitiques peralumineux et les gîtes de la région de Bonnac. La formation de la minéralisation entre 321-316 Ma est contemporaine à légèrement plus jeune que celle des dykes peralumineux mis en place autour de 329-315 Ma, ce qui suggère une genèse lors d'une transition magmatique-hydrothermal. Dans ce modèle, le refroidissement d'un pluton granitique à deux micas sous-jacent, pourrait générer des fluides magmatiques et servir de source de chaleur activant une circulation du fluide vers des zones à haute perméabilité comme des fractures préexistantes. Le fluide magmatique aurait ensuite été rééquilibré à haute température par des processus d'interaction fluide-roches. Les changements brusques de pression, la baisse des températures, et de fugacité du soufre générés par un apport tardif de fluides météoriques semblent responsables du dépôt du stade aurifère tardif. À l'échelle régionale, l'événement or-tungstène est attribué à un stade hydrothermal précoce, et dissocié de la formation de l'événement à antimoine du district. La mise en place des dykes leucogranitiques et des veines de quartz de Bonnac est contrôlée par une direction d'étirement NW-SE, interprétée comme une expression de l'extension syn-orogénique d'âge Serpukhovien-Bashkirien (événement D4 du Massif Central français). Ces nouvelles données fournissent des preuves d'une première période métallogénique à tungstène et or dans le FMC avant l'événement «Or 300». La classification génétique des minéralisations de Bonnac est équivoque. Les veines de quartz à W-As-Bi-Au présentent à la fois les caractéristiques du modèle de "l'or orogénique", avec un niveau relativement profond de mise en place (mésozonal), et celles du modèle Intrusion-Related-Gold-Deposit (IRGD) avec un lien spatio-temporel entre la minéralisation et une intrusion peralumineuse. Nous proposons que Bonnac soit un type intermédiaire entre un modèle typique de l'or orogénique, et un IRGD. Nous soutenons que la présence de teneurs économiques en or

dans les gisements de tungstène de type filonien, et plus généralement ceux de type IRGD, ont été sous-estimés dans la partie varisque du Massif Central Français.

Mot clés : Minéralisation à Tungstène-Or, Massif-Central-Français, IRGD, métallogénie Varisque, district de Brioude-Massiac, Age U-Pb sur apatite.

1. Introduction

The French Massif Central (FMC) represents a prominent metallogenic province for gold (Bouchot *et al*., 2005) but only a few tungsten deposits have been found, although resources of at least 45,000t of WO_3 have been estimated, (Audion and Labbé, 2012), this is probably the consequence of an under-exploration for this metal in the FMC. The ubiquity of the quartz-wolframite hydrothermal veins makes it the main source of tungsten in the FMC. Some deposits with still a strong economic potential were formerly mined, such as Leucamp, Enguialès and Echassières (Marignac and Cuney, 1999; Fig. 1).

Among the wolframite-bearing veins of the FMC, some display a polymetallic content with bismuth and gold in sub-economic grade (W-As-Bi-Au). They are ascribed either to the perigranitic wolframite vein-type (Marignac and Cuney, 1999) or to orogenic gold deposit (Bouchot *et al*., 2005). In the FMC, occurrences of W-As-Bi-Au are known in gold mining districts such as the Limousin (Marcoux and Bonnemaison, 1988), Pontgibaud (Marcoux and Picot, 1985), Brioude-Massiac (Périchaud, 1970; Bril, 1982; Marcoux and Bril, 1986; Sandras, 1988; Bril and Beaufort, 1989; Bril *et al*., 1991), Montredon (Béziat *et al*., 1980), S^t-Mélany (Charonnat, 2000; Chauvet *et al.*, 2012), and Leucamp districts (Derré, 1983; Bogdanoff *et al.*, 1987; Demange *et al.*, 1988; Bouchot *et al*., 2005; Lerouge and Bouchot, 2009). The spatial association of the wolframite-quartz veins with Carboniferous peraluminous two-mica granites

argues for an important role of this crustal magmatism in the genesis of the tungsten mineralization (Marignac and Cuney, 1999, Cuney *et al.*, 2002; Bouchot *et al*., 2005; Harlaux *et al*., 2018). However, the formation of these peri-granitic deposits is still debated. In particular, the temporal and genetic links between the episodes of magmatism, deformation, and hydrothermal mineralization are not fully clarified.

U-Pb TIMS dating on wolframite from the Limousin, Echassières, Montredon, and S^t-Mélany districts (Fig. 1) has been recently performed (Harlaux *et al*. 2018). The obtained U-Pb ages define the existence of three tungsten mineralizing events closely related to magmatic activity: i) Visean to Serpukhovian mineralization (333 – 327 Ma) coeval with the emplacement ages of large peraluminous two-mica plutons (ca. 335 – 325 Ma) during the syn-orogenic extension, ii) Serpukhovian to Bashkirian mineralization (317 – 315 Ma) synchronous with the emplacement of syn-tectonic granites (ca. 315 – 310 Ma) during the late-orogenic extension, iii) Gzhelian to Asselian mineralization (around 300 – 298 Ma), formed during the post-orogenic extension, coeval with the metallogenic peak of the Or300 event during which the main orogenic gold deposits were emplaced in the FMC (Bouchot *et al*., 2005).

In the central part of the FMC, i.e. in the Pontgibaud, Brioude-Massiac, and Leucamp districts, the timing for the emplacement of the wolframite bearing veins remains poorly constrained. Furthermore, the genetic relationships between the ore deposits and the granitic emplacement is not yet demonstrated. The Bonnac area, in the central part of the Brioude-Massiac district is a good target to address these questions (Fig. 1). Indeed, in this area, a dozen of W-As-Bi-Au bearing quartz veins from the South of the Bonnac village to the Scoufour hamlet (Fig. 3) further north (Périchaud, 1970; Sandras, 1988) are spatially associated with a leucogranitic dyke swarm dated at 322 ± 7 Ma (K/Ar on muscovite, Bril *et al*., 1991), while the W-As-Bi-Au mineralization yields late Permian age of about 250 Ma (K/Ar on muscovite from Bonnac; Bril *et al*., 1991). Variable gold grades ranging from 1 to 15 g/t have been reported in

ore samples from the region (Périchaud, 1970; Sandras, 1988), but the relationship between gold and tungsten ore is not clearly documented.

The aim of this study is to better understand the W-As-Bi-Au quartz vein deposits in the FMC, and more particularly in the Bonnac area. It focuses on the structural control and the timing of these ore deposits, and their relationships with the Carboniferous tectonics and magmatism, and will be integrated within the hydrothermal framework of the Variscan FMC. Detailed field structural studies, and in-situ apatite LA-ICP-MS U/Pb dating were carried out. Mineralogical and geochemical studies were also performed to decipher the tungsten-gold relationships and propose an updated metallogenic model.

2. Geological and metallogenic background

2.1 The Haut-Allier area in the FMC Variscan framework

Located in the central part of the FMC, the 1000 km^2 Brioude-Massiac polymetallic district is covered by Cenozoic basaltic flows, and bounded to the northeast by the Oligocene Limagne graben. The district that belongs to the Variscan orogen, is a N120-130°E trending antiform that refolds the stack of metamorphic nappes recognized in the entire Massif Central (e.g. Burg and Matte, 1978; Ledru *et al*., 1989; Faure *et al*., 2005, 2009; Fig. 1, 2). The core of the area is occupied by the Lower Gneiss Unit (LGU) represented by biotite-sillimanite paragneiss, intruded by the Céroux orthogneiss derived from a Cambro-Ordovician alkaline granite (Burg and Matte, 1978; Lasnier *et al*., 1982; Mathonnat, 1983; Thonat *et al*., 2014). The LGU is tectonically overlain by the Upper Gneiss Unit (UGU), which is formed by migmatitic paragneiss with rare orthogneiss, and a felsic-mafic association called the "leptynite-amphibolite complex". The mafic rocks experienced an eclogite-facies or granulite-facies metamorphism during the eo-Variscan evolution (Marchand, 1974; Lasnier, 1977; Bernard-Griffiths *et al*., 1980).

171 The nappe stacking in the Haut-Allier area was probably acquired during the early
172 Carboniferous, around 350-340 Ma (monazite U/Pb dating on syntectonic granulite; Pin and
173 Peucat, 1986). Then two extensional events, coeval with granitic intrusions accommodated the
174 crustal thinning widely observed in the FMC (e.g. Malavieille *et al.*, 1990; Faure and Pons,
175 1991; Faure, 1995). i) The syn-orogenic extension at ca 330-310 Ma, called D4 event (Faure *et*
176 *al.* 2009), is characterized by a NW-SE maximum stretching recorded by the syn-tectonic
177 biotite monzogranite and the two-mica granite plutons and their country rocks. In the Brioude-
178 Massiac area, andalusite-leucogranitic dykes and their related two-mica granites (Sandras,
179 1988; Bril *et al*., 1991) belong to this D4 event. ii) The late-orogenic extension (D5 event,
180 between 310 to 299 Ma; Faure *et al*., 2009), with a NNE-SSW maximum stretching direction,
181 was contemporaneous with the emplacement of highly differentiated peraluminous intrusions
182 and pegmatites, and rare-metal granites (Cuney *et al*., 2002). The opening of the Late
183 Carboniferous coal basins belongs to the D5 event (Faure, 1995).
184
185 2.2 The Bonnac W-As-Bi-Au deposits

186 The study area is located in the central part of the Brioude-Massiac polymetallic district
187 which contains more than 200 veins-type deposits and occurrences with variable ore content:
188 W, Sn or W-As-Bi-Au (Bonnac, Vèze-Bosberty veins), Sb (Au), Pb-Zn or F and Ba (Fig. 2).
189 Antimony veins have been the main economic substance mined between 1850 and 1978 with
190 an historical production of 43 000 t Sb metal (Périchaud, 1970; De Gramont *et al*., 1990). The
191 Bonnac area was only mined for gold between 1880 and 1911 with a production of only 2 kg
192 of gold, and never for tungsten (Périchaud, 1970; De Gramont *et al*., 1990).

193 The Bonnac W-As-Bi-Au quartz-veins are spatially associated with Sb (Au) quartz veins
194 (Fig. 2) and are located in the southwestern limb of a regional N120-130°E antiform. All veins
195 seem to crosscut the foliation of the LGU paragneiss (Fig. 2 and 3). Some quartz veins develop

196 immediately at the contact with andalusite leucogranitic dykes (Périchaud, 1970; Sandras,
197 1988). The ore mineralogy, is mainly represented by arsenopyrite-löllingite with wolframite,
198 minor scheelite, associated with bismuthinite, native bismuth, tetradymite and visible gold in a
199 quartz gangue with muscovite clusters (Périchaud, 1970; Bril, 1982; Bril and Beaufort, 1989).
200 Detailed studies on fluid inclusions (Bril, 1982), hydrothermal alteration (Bril and Beaufort,
201 1989), and lead isotopic signature (Marcoux and Bril, 1986) allow to constrain the P-T
202 conditions of vein deposition. The Bonnac veins display two successive hydrothermal stages
203 with an early high temperature (homogenization temperatures between 350-400 °C) CO_2-CH_4-
204 rich ± N_2 aqueous fluid with low-salinity (about 5 equiv wt % NaCl), interpreted as of
205 metamorphic origin, and a late low temperature (homogenization temperatures between 200 –
206 300 °C) aqueous fluid, with low-salinity, of meteoric origin, similar to the ore forming fluid
207 from the Sb (Au) deposits. According to the same authors, the formation of the W-As-Bi-Au
208 and Sb (Au) veins could be contemporaneous, the result of a single hydrothermal system coeval
209 with the emplacement of an underlying, albeit hidden, Permian pluton. The ore veins were
210 considered to show a zonal distribution, with W-As-Bi-Au occurring in a limited area, near the
211 intrusion, the Sb (Au) veins being more distal.

212 2.3 The intrusive rocks

213 Leucogranitic dykes, striking N30°E, N60°E and sometimes N100°E, with a variable
214 thickness (between 50 cm to 20 m), and small extension (less than 3 km), are cropping out in a
215 few clusters in the district, the Bonnac area being one of the most important (Fig. 2 and 3).
216 These dykes display a homogeneous mineralogical and chemical composition in the overall
217 district (Sandras, 1988). Quartz is the most abundant mineral, associated with plagioclase, and
218 sub-euhedral K-feldspar (< 5 mm) with biotite aggregates and muscovite. Andalusite is
219 observed as small sized grains (0.6 to 0.8 mm), associated with the K-feldspar and quartz. A
220 temperature emplacement of ca 600-650 °C, and a pressure of 0.4 GPa, was estimated from the

andalusite-quartz assemblage (Sandras, 1988). An emplacement age of 322 ± 7 Ma was documented by K/Ar radiometric dating on muscovite (Bril *et al*., 1991).

The dykes chemical compositions correspond to a peraluminous two-mica granite with 74 to 76 % SiO_2, and a Al2O3/CaO+Na2O+K2O ratio up to 1.6 (see EDM. 1 for analytical details). This bulk chemistry is similar to those found in the Chatelet gold district, and other Visean to Serpukhovian leucogranites from the Limousin district (e.g. S^t-Sylvestre massif; Scaillet *et al*., 1996). A local partial melting of the LGU paragneiss could be responsible for the genesis of those intrusive rocks (Sandras, 1988). A spatial and potentially genetic link with the W-As-Bi-Au deposits of the Brioude-Massiac district is assumed. At Bonnac, the dykes are interpreted as the shallow expression of an underlying pluton (Sandras, 1988; Bril and Beaufort, 1989).

3. Materials and methods

The accessory mineral phases were identified using a Merlin compact Zeiss Scanning Electron Microscopy (SEM), co-operated by BRGM-CNRS-Orléans University, and equipped with Energy Dispersive System (EDS) for qualitative analyses. In addition, SEM-cathodoluminescence images have been made using MEB-CL MIRA-3 Tescan (BRGM-CNRS-Orléans University). Chemical analyses of arsenopyrite were obtained with the Cameca SX-Five Electron Probe Micro-Analyzer (EPMA) at the Institut des Sciences de la Terre d'Orléans (ISTO). Analyses were performed using an accelerating voltage of 20 kv, a beam current at 40 nA, a beam diameter of 3 µm, and a counting time of 30 s for Fe, Ni, Co, Sb, Pb, Cu, As, Zn, Ag, Bi, and 60 s for gold. Details on the method, parameters and analytical data are given in ESM2.

U/Pb dating on hydrothermal apatite from the mineralization was conducted in-situ by laser ablation inductively coupled plasma mass spectrometry (LA-ICP-MS) at the GeOHeLiS analytical platform (Géosciences Rennes/OSUR, Univ. Rennes) using an ESI NWR193UC

Excimer laser coupled to an Agilent 7700x quadrupole ICP-MS equipped with a dual pumping system to enhance sensitivity (Paquette *et al*., 2014). The analytical procedure followed the method described in Pochon *et al*. (2016). Details, standards analyses and analytical data are provided in ESM3. All errors are listed at 2σ level. Concordia diagrams and calculated ages have been produced using IsoplotR (Vermeesch, 2018).

4. Field characterization of the W-As-Bi-Au quartz veins

4.1 Field and structural features from the Bonnac area

The strike of the mineralized quartz veins displays three different orientations similar to those of the leucogranitic dykes. The N30°E trend is represented by the Riolet, Androl, Rode, Borie veins), the N60°E by the Costillon one, while few veins strike N90°E and N160-170°E (Fig. 3). The vein dip varies between 30° to 45° to the SE whatever their strike. Mineralized quartz veins are located in the hangingwall or footwall of the leucogranitic dykes (Fig. 4, 5). They display similar features all around the area, with a lenticular shape, and a narrow width of 1 to 20 cm. The host-rocks are weakly affected by the hydrothermal alteration. The geometric relationships show that the leucogranitic dykes crosscut the paragneiss foliation, and are cut by the mineralized veins (Fig. 4B, 5) with locally developed breccias (Fig. 4B).

Most of the vein wallrocks are fault planes with a down-dip striation, indicating a normal motion (Fig. 5). Some veins display also a striation with a NE 40-50° pitch, in which quartz steps indicate a normal component of displacement (Fig. 5C, D). The observed kinematics of the Costillon vein (Fig. 4A) also indicate a normal motion that complies with the drag folds asymmetry developed around the leucogranitic dykes (Fig. 5B). Late N60-65°E striking sub-vertical barren faults, with gouge, offset the quartz veins (Fig. 4A).

4.2 Field and structural features from the Scoufour-area

The Scoufour mineralized quartz veins exhibit some differences with the Bonnac ones. Three N10-30°E striking low-angle veins with a dip between 10 and 20° to the SE are observed (Fig. 6). Their thickness is comprised between 30 and 50 cm, but may exceed 1m. Here, leucogranitic dykes are absent, and the host-rock underwent a hydrothermal alteration related to the mineralization. A greisen-type alteration is thus observed up to 1 or 2 m from the vein, resulting in the bleaching of the paragneiss by transformation of biotite into muscovite with associated silicification. Drag folds observed near the Ferbert vein show a normal motion (Fig. 6B). A late fracturing event, represented by N20-25°E steeply NW dipping barren faults with gouge, is also recognized (Fig. 6A).

All the structural features observed in the Bonnac and Scoufour areas are summarized in Figure 7. In both cases, the emplacement of the mineralized quartz veins occurred during a single deformation phase coeval with a hydrothermal event. The magmatic event responsible for dyke emplacement post-dated the regional metamorphism but preceded the ore veins emplacement. Furthermore, normal faults rework the pre-existing faults that controlled the emplacement of the leucogranitic dykes. Lastly, both dykes and mineralized veins are cut by NE-SW subvertical faults with subhorizontal striation indicating a sinistral motion.

5. Mineralogy and geochemistry of the W-As-Bi-Au ore veins

5.1 The mineralized facies

All the mineralized veins of the study area have similar habitus, with a massive infill of coarse white-grey quartz gangue with parallel ribbons of a few centimeters, or aggregates of arsenopyrite and coarse wolframite (Fig.4A and 8). Secondary scheelite is common in cm-scale pseudomorphic aggregates of early wolframite that may appear as rare relicts and rarely observed as isolated, coarse grains or infilling fractures. (Fig. 8).

293 On the basis of gangue and ore mineral textural observations, 3 stages have been recognized,
294 namely: i) stage 1 with tungsten and arsenic, ii) stage 2 with arsenic, and tungsten, iii) stage 3
295 with bismuth, gold, and base metals.

296 5.2 Stage 1: early tungsten and arsenic

297 The first opening of the veins corresponds to the deposition of a wolframite and löllingite
298 assemblage in a macrocristalline Qz1 quartz (crystal size > 500 µm; Fig. 9A, B). Observed with
299 cathodoluminescence, Qz1 displays a blocky habitus with regular growth bands without
300 significant deformations (Fig. 9B), and numerous fluid inclusions. Coarse euhedral wolframite
301 crystals (up to 1 cm) are associated with cm-size aggregates of löllingite (Fig. 9A). SEM
302 analyses of wolframite exhibits a high iron grade (6-8 wt %) and a lower manganese one
303 suggesting a ferberite. Large apatite crystals (> 100 µm) have been observed within Qz1 in
304 close association with wolframite (Fig. 9C). Their euhedral shape and straight grain boundaries
305 suggest it is coeval with Qz1.

306 5.3 Stage 2: arsenic and late tungsten

307 The beginning of stage 2 is marked by an intense and heterogenous episode of deformation
308 (Fig. 9A, B, C, D) which has affected the previous stage 1 assemblage. Qz1 grains experienced
309 a dynamic recrystallization (Stipp *et al*., 2002) shown by undulose extinction, subgrain rotation
310 and recrystallization with golfed or jagged shape of the Qz1 boundary, bulging and quartz
311 neograin (Qz2) formation at the expense of the early Qz1 (Fig. 9 B, D and Fig. 10 A and B).
312 Qz2 displays undulose extinction and grain size reduction and is located along 10 to more than
313 500 µm shear bands that surround the edges of Qz1, or crosscut it.

314 The crystallization of arsenopyrite (Fig. 9 B) and scheelite are coeval with the deformation
315 episode. Arsenopyrite forms small rhombic crystals (up to 100 µm) and fills the fracture
316 network of the stage 1 löllingite or wolframite and sometimes totally pseudomorphs after

löllingite. Xenomorphic scheelite forms at this stage by partial or total pseudomorphosis of previous wolframite (Fig. 9 A, C).The scheelites, show rare inclusions of niobium oxides rich in niobium as on the Ferbert vein, (65 wt % Nb_20_5), iron (25 wt % FeO), manganese (4.5 wt % MnO), tungsten (2.4 wt % WO_3), titanium (2.2 wt % TiO_2) and scandium (0.9 wt % Sc_2O_3). Those uncommon oxides have been observed in the Puy-Les-Vignes tungsten deposit (Harlaux *et al*., 2015).

The 56 EPMA analyses of arsenopyrite (see Table 1 and ESM 2 for detail) have been compared with previous study of Bril (1983) from the Bonnac area and from other W-As-Au regional veins (Vèze and Bosberty, see Fig. 2 for localization). Arsenopyrite has a very similar composition in all deposits with As % average values of 33.4 %, 32.8%, and 33.0 % for Bonnac, Vèze, and Bosberty veins, respectively. Minor elements, e.g. Co, Ni, Sb, Au are under the detection limit of the method. According to Kretschmar and Scott (1976), and Sharp *et al*. (1985), the use of the arsenopyrite chemical compositions to assess ore formation temperatures may be considered with a good confidence level, because of the absence of minor element. Assuming the arsenopyrite-pyrrhotite equilibrium, the calculated formation temperature was around 480 °C. These values are in the same range than those deduced from the H_2O-CO_2 L1-type fluid-inclusions (homogenization temperature between 300 and 420 °C; Bril, 1982).

5.4 Stage 3: Bi-Te-Au and base metals

This stage is marked by the deposition of a new discrete quartz generation (Qz3) in the fractures of arsenopyrite or löllingite (Fig. 10 C, D). The medium grain-size (around 100 µm) Qz3 displays a subeuhedral shape or elongate-fibrous habitus. Its hyaline aspect is due to the scarcity of fluid and solid inclusions. This Qz3 never experienced dynamic recrystallization (Fig. 10 C, D) and is coeval with a bismuth-telluride-gold-base metals assemblage (Fig. 10 C, D, E). Rhombic arsenopyrite crystals are commonly crosscut by large mm-size, subeuhedral

342 pyrite, associated with bismuth-telluride and base-metals minerals (Fig. 11 D, E). The EPMA
343 chemical analysis of the pyrite from Bonnac veins does not show minor element.

344 Bismuthinite and native bismuth are the dominant minerals species of this stage 3. They
345 occur as 2 to 80 µm inclusions aligned along the cleavage plane of löllingite (Fig. 11A), also
346 within arsenopyrite, or wolframite (Figs. 10 C, D; 11 A, B, C), and as small-size aggregates (<
347 500 µm) or in fractures crosscutting löllingite or arsenopyrite (Fig. 10E, F). Native bismuth is
348 frequently observed as ovoidal inclusions within bismuthinite (Figs. 10 F; 11 C). Xenomorphic
349 hedleyite (Bi_7Te_3) is the main tellurium mineral, always closely associated with the
350 bismuthinite and native bismuth. Tetrahedrite [$(Cu,Fe)_{12}Sb_4S_{13}$] and a bismuth-antimony-
351 sulfide, close to the chemical composition of the horobetsuite [$(Bi,Sb)_2S_3$, have been identified
352 as inclusions in a hedleyite aggregate (Fig. 10 F). In the Ferbert vein, a late deposition of Cu-
353 Zn-Pb minerals overprints and brecciating all the previous minerals. Chalcopyrite is the main
354 mineral, with small tetrahedrite inclusions (50 µm). Sphalerite and minor galena complete this
355 assemblage. This late deposition stage is associated with a Qz4 quartz generation displaying
356 undeformed pyramidal grains (Fig. 11E).

357 Visible gold has been commonly observed in thin-sections from all veins of the Bonnac area.
358 Most of the gold intergrowths with the Bi-Te minerals, (Fig. 10 B, 11 A, B, C), or more rarely
359 appears within sulfides (mainly chalcopyrite, Fig. 11 D, E), or sometimes pyrite or isolated
360 between Qz2 grains. Gold patches range between 1 µm to 25 µm in size but can reach 50 µm
361 within sulfides. All display a xenomorphous rounded shape (Fig. 11). Rare maldonite (Au_2Bi)
362 has been observed by SEM analysis as a few microns inclusions intergrowths with native
363 bismuth.

364 Ten EPMA analyses of gold grains intergrowths with native bismuth and within chalcopyrite
365 from the Ferbert vein are provided in Table 1 (see EDM 2 for detailed analyses). The small size

366 of the gold grains explains why the analyses do not reach 100 %. Silver is the only element
367 present with gold (average of 16.7 wt % Ag). “Gold” of Bonnac area is thus an electrum with
368 a gold fineness of 830 (Morisson *et al*., 1991).

369 The three economic-stages described above are summarized in figure 12, however, this
370 evolution represents increments of a single progressive crystallization-deformation event.
371
372 It should be noted that, a poorly developed and uneconomic post-ore stage, macroscopically
373 highlighted by a dark-gray quartz facies, has been only observed in the Ferbert vein. All the
374 previous stages are brecciated and cemented by a chalcedonic quartz gangue with minor
375 carbonates. The associated metallic-minerals are pyrite-marcasite aggregates with pyrrhotite
376 relics, with a new generation of chalcopyrite, and sphalerite. This does not greatly affect the
377 previous assemblages.
378

379 **6. LA-ICP-MS U/Pb geochronology on apatite**

380 Hydrothermal apatite from the early tungsten-arsenic stage 1 (Fig. 9C and Fig. 12) of the
381 Androl (Bonnac area) and Ferbert veins (Scoufour area) have been carefully characterized and
382 15 grains have been selected for dating. Namely, 9 from the Ferbert vein (mineralized quartz
383 vein sample BM46D) and 6 from Androl vein (mineralized quartz vein sample BM39A; ESM
384 3 for analytical details). The cathodoluminescence image shows growth zones without evidence
385 complex zoning (Fig. 13 A, B). Between 2 and 6 U/Pb analysis have been performed on each
386 grain (Fig. 13C, D). Apatite grains from the Ferbert vein have variable $^{207}Pb/^{206}Pb$ ratios,
387 ranging between 0.1849 and 0.7010. The discordant points plot along a discordia line that yields
388 a lower intercept date of 315.6 ± 2.8 Ma (MSWD = 3.7; Fig. 13C). The data plot along a
389 discordia line yielding a lower intercept date of 323.4 ± 3.2 Ma (MSWD = 2.4, Fig. 13D). The
390 intersect point of the discordia give the isotopic composition of the initial lead of the dated

391 apatite (Fig. 13C, D). Their composition shows some difference between the Ferbert vein and
392 the Androl vein with respectively 0.823±0.005 and 0.853±0.013. Those results are consistent
393 with initial $^{207}Pb/^{206}Pb$ ratios measured in different nearby mineralized veins, and main
394 lithological formations of the Brioude-Massiac area (Marcoux and Bril, 1986). Thus, the
395 Fournial (Pb-Ag-Sn-As veins) have $^{207}Pb/^{206}Pb$ ratios different 0.86234±0.00027 (n=14), but
396 that of the Sb-(Au) vein of the Céroux is closer 0.8598±0.0014 (n=1). On the other Sb-(Au)
397 veins, the isotopic compositions of the lead remain variable within de district. The aplitic dykes
398 close to a leucogranitic composition from the la Margeride pluton, in the southern part of the
399 district, show the strongest correlation with the Androl vein with a $^{207}Pb/^{206}Pb$ ratio of 0.8569
400 (n=1, composition recalculated at 320 Ma).

401 **7. Discussion**

402 7.1 Mechanisms of ore-vein formation and chemical-thermal evolution

403
404 During **stage 1**, the initial vein opening, coeval with the massive crystallization of the Qz1
405 under low-strain, was contemporaneous with a high temperature (up to 400 °C) paragenesis
406 with wolframite and löllingite from an As and W enriched fluid with low-salinity (about 5 equiv
407 wt % NaCl) CO_2-CH_4-rich ± N_2 aqueous fluid (V-type fluid inclusions in the classification of
408 Bril, 1982).

409 A ductile/brittle deformation episode marks the beginning of **stage 2** (Fig. 12). The first Qz1
410 experienced a dynamic recrystallization shown by undulose extinction, subgrain rotation
411 recrystallization, bulging and quartz neograin (Qz2) formed at the expense of the early Qz1.
412 Ductile/brittle deformation features argue for a deep-seated formation between 12 to 9 km
413 (Scholz, 1988). This is supported by the range of temperature for this stage, estimated around
414 480 °C, based on the arsenopyrite thermometry and, in agreement with the estimated
415 temperature range (400 to 500 °C) deduced from the quartz textural observations (e.g. Stipp *et*

al., 2002). Those depth and temperature estimation are in good agreement with the estimated emplacement conditions of the leucogranitic dykes of Bonnac (see part 2.3). The transformations of wolframite into scheelite, and löllingite into arsenopyrite suggest a change in fluid chemistry, still rich in As and W, and marked by an increase in sulfur fugacity and in the calcium activity. The pseudomorphic textures argue for a remobilization of the tungsten from the previous ferberite. The increase of the Ca/Fe ratio in the fluid, associated with a slightly decrease of the temperature, as predicted by Wood and Samson, (2000) could possibly correspond to higher fluid interaction with the surrounding metamorphic formations. This fluid could correspond to the L1-type fluid inclusions defined by Bril, (1982), with low-salinity (3.5-0 equiv wt % NaCl), lower CO_2 aqueous fluid, and trapping temperature estimated around 300 to 400 °C (Fig. 14).

The onset of **stage 3** (Fig. 12) was marked by brittle fracturing. The previous assemblage was micro-brecciated, and invaded by a hyaline, low-strain Quartz (Qz3). This new quartz generation was coeval with the deposition of native bismuth, bismuthinite, hedleyite, electrum, pyrite, and base-metals minerals (chalcopyrite, sphalerite, galena). The microcrack infill as well as fluid and solid-inclusions bands (Fig. 10 A, B) suggest fluid-assisted fracturation under a hydrostatic regime at a depth comprised between 7 and < 5 km (Scholz, 1988). This stage 3 might be interpreted as a consequence of a crack-and-seal trigged by a fluid overpressure mechanism (Ramsay, 1980). The emplacement of the previous massive quartz generations could have sealed the porosity in the fault zone and act like an impermeable barrier to fluid flow allowing an increase in the fluid pressure. The crack-and-seal process has triggered pressure drop from lithostatic to hydrostatic regime, and might be interpreted as a consequence of a fault-valve mechanism (Sibson *et al*., 1988; Cox *et al*., 1991; Robert *et al*., 1995; Gaboury and Daigneault, 2000). The textural evolution reflects the transition from a lithostatic pressure context during stages 1 and 2 with a limited permeability to pervasive fluid circulation in

connected fractures, therefore implying a transition from, an aseismic to, a seismic environment (Cox, 1987; Cox *et al*., 1991).

The deposition temperature of gold during stage 3 can be deduced from the paragenetic association of native bismuth and bismuthinite. According to Barton and Skinner (1979), a range of temperature between 320 to 240 °C can be proposed. However, the association of native bismuth and hedleyite can only be stable below a temperature of 266°C (Dimitrova and Kerestedjian, 2006). Therefore, we propose a temperature range between 266 to 240 °C for the deposition of stage 3, which is in good agreement with a ca 200 °C homogenization temperature deduced from the L2-type secondary aqueous fluid inclusions (Bril, 1982). This relatively low temperature accounts for the deposition of antimony-rich Bi-Te minerals like the horobetsuite or the tetrahedrite.

7.2 Possible mechanisms for gold deposition

The common occurrence of electrum within Bi-Te minerals might emphasize the role of a polymetallic melt/liquid for the concentration of precious metal, as already reported for similar mineralization (Ciobanu *et al*., 2006; Cook *et al*., 2007; Ciobanu *et al*., 2010; Zacharias *et al*., 2014). The polyphase character of the ore-inclusions (electrum intergrowth in native bismuth, or electrum, native bismuth intergrowths in hedleyite), the ovoidal shape of the electrum inside native bismuth, and the presence of minerals such as maldonite or horobetsuite might support this mechanism (Ciobanu *et al*., 2006; Zacharias *et al*., 2014). But our deposition temperature estimate, between 266 to 240 °C, is too close to, or even below, the bismuth solidus temperature, and the eutectic temperature of the Au-Bi system (241 °C). This leads us to suggest that a large part of the gold and Bi-Te phases probably precipitated directly form a hydrothermal fluid enriched in Bi-Te-Au and were not scavenged by a bismuth-rich liquid/melt.

Between stages 1 and 3, a temperature decrease is observed (Fig. 14). In addition, the stage 3 underwent a significant pressure drop associated with a change in tectonic regime, which might have triggered the input of a meteoritic fluid (Bril, 1982; Fig. 14). Furthermore, the decrease in the sulfide activity in the ore-fluid could be responsible for the gold deposition by destabilization of gold-sulfide complexes associated with the ongoing sulfide precipitation (Williams-Jones *et al*. 2009).

7.3 Tectonic control and timing of ore deposits within the Variscan evolution framework for the French Massif Central

The vein geometry observed in the field is controlled by the inherited structures. The medium dip (30-50° SE) of the Bonnac veins reused the previous fault system coeval with dyke emplacement, whereas the low-angle dip Scoufour veins are controlled by the host-rock foliation. These anisotropy surfaces can be easily reactivated during faulting, and channeled the ore-bearing fluids.

Kinematic data on the striated fault planes coeval with W-As-Bi-Au veins allowed us to derive the stress tensor by an optimized inversion method (Delvaux and Sperner, 2003). The result indicates an extensional tectonic regime with the maximum (σ_1), intermediate (σ_2), and minimum (σ_3) principal stress axes oriented 39°E/86°, 37°E/04° and 127°E/0°, respectively (Fig. 15). The W-As-Bi-Au quartz veins deposition was controlled by a NW-SE horizontal extension direction, consistent with the NW-SE stretching direction documented for the D4 tectono-magmatic event in the FMC (Faure, 1995). This widespread event, related to the syn-orogenic Variscan extension in the FMC, dated between 325 and 310 Ma, is contemporaneous with the emplacement of the leucogranitic and monzogranitic syn-tectonic plutons (Figs. 1, 16;

489 Faure and Pons, 1991; Faure 1995; Faure *et al*., 2009; Talbot *et al*., 2005a, 2005b; Joly *et al*.,
490 2007, 2009).

491 The hydrothermal apatite grains from two localities in the Bonnac area yield LA-ICP-MS
492 U/Pb dates of 315.6 ± 2.8 for the Ferbert vein (Scoufour area) and 323.4 ± 3.2 Ma for the Androl
493 vein (Bonnac area), respectively interpreted as the emplacement age of the W-As-Bi-Au veins.
494 This age of ca. 320 Ma is consistent with the D4 tectonic, which is also coeval with the
495 Serpukhovian-Bashkirian generation of tungsten ore deposits with minor gold in the FMC as
496 the Puy-les-Vignes or S^t-Mélany (Fig. 16; Harlaux *et al*., 2018). Closer to the Brioude-Massiac
497 district, the Leucamp and Enguialès ore deposits in the Châtaigneraie district yielded the most
498 important tungsten resources of the FMC (Derré, 1983; Bogdanoff *et al.*, 1987; Demange *et al.*,
499 1988; Lerouge and Bouchot, 2009) are other examples of this tungsten ore deposition event.

500 All previous works (Périchaud, 1970; Bril et Beaufort, 1989) in the Brioude-Massiac district,
501 proposed a single hydrothermal event, responsible for the formation of both antimony and
502 tungsten-gold from a perigranitic metal zonation. This model seems to be challenged by our
503 results. Despite their spatial link with the antimony veins, the W-As-Bi-Au ones yield a distinct
504 age, since the antimony veins of the Brioude-Massiac district belong to a younger hydrothermal
505 event referred to as the "Or 300" event (Bouchot *et al*., 2005; Cheval-Garabédian, 2019). We
506 have shown that the Bonnac W-As-Bi-Au mineralizations have a polyphased history in a
507 continuum of time (Fig. 12), which fits with a unique deformation event, decorrelated with the
508 Or300 event. The three mineralized stage are all trapped in quartz-veins with same and distinct
509 structural control (D4 tectonic event), same kinematics, a same infilling chronology with a
510 continuity from a ductile/brittle to only-brittle regime, associated with a progressive cooling of
511 the ore-fluid (Fig. 12 and 14), and by the absence of late remobilization textures during the gold
512 stage 3. This, is also attested by the obvious age difference.

Our results, together with the emplacement ages obtained on the gold-bearing quartz veins from the Cévennes district (Chauvet *et al*., 2012) argue for an earlier Bashkirian-Moscovian gold-hydrothermal event, sometimes associated with tungsten, during the D4 event. Our data allow us to propose a polyphase history in the FMC characterized by two distinct hydrothermal events carrying gold, namely: i) a first Serpukhovian to Bashkirian, and, ii) a second, Gzhelian-Asselian, as the Or300 event, that might have re-used the structural discontinuities that controlled the early event. Recent new data obtain on the orogenic-gold deposit of the la Bellière district (Armorican Massif) argue also for a tectonic-hydrothermal gold event earlier than the Or300 event around 340-325 Ma (Cheval-Garabédian *et al*., 2020).

7.4 Genetic link with the Serpukhovian leucogranites and ore deposit model for the Bonnac area

Based on our results, the genetic relationships between the mineralization and the leucogranitic dykes can also be re-assessed. The leucogranitic dykes from Brioude-Massiac, dated at 322 ± 7 Ma (Bril *et al*., 1991) were emplaced contemporaneously with the D4 event and are spatially related to the W-As-Bi-Au deposits. The mineralizing event that followed the intrusive rocks emplacement could be interpreted as a magmatic-to-hydrothermal evolution (Fig. 17; Linnen and Cuney. 2005; Gloaguen, 2006) with a relatively long-time duration, around 329-316 Ma (dating of the leucogranitic magmatic event). Several lines of evidence support this interpretation as: i) the spatial and temporal link between dykes and mineralized veins; ii) their formation during the D4 tectonic event; iii) the high temperature paragenesis of stage 1 at 400-500 °C, close to the 600-650 °C emplacement temperature estimated for the andalusite-leucogranitic dykes, iv) their close emplacement depths estimated around 10 km (Sandras, 1988), v) the reworking of previous structural discontinuities. Throughout the Variscan Orogen,

538 there are examples of W-Au deposits that were emplaced within a time gap of ca. 10 Ma after
539 the intrusions of peraluminous magmas (Romer and Kroner, 2016). In France, the Puy les
540 Vignes deposit (Harlaux *et al*., 2018), and the Salau deposit in the French Pyrenees (Poitrenaud
541 *et al*., 2019), or in the Bohemian Massif, the Mokrsko deposit (Zacharias *et al*., 2014), are good
542 examples of this relation.

543 A two-stage evolutive model for the magmatic-hydrothermal system in the Bonnac area is
544 proposed in a continuum of time (Fig. 17). Between 329 and 315 Ma, the emplacement of
545 leucogranitic dykes, related to an underlying pluton, was controlled by normal faulting in the
546 regional NW-SE extensional regime. Slightly younger from the dyke crystallizations, between
547 321 to 316 Ma, the deformation became more localized and contemporaneous with quartz veins
548 emplacement that recorded a magmatic-to-hydrothermal transition (Fig. 17 stage 2). These
549 hydrothermal fluids have reused the previous discontinuities as feeder channels.

550 The metamorphic or magmatic origin of the ore-forming fluid for peri-granitic ore deposits
551 is still a matter of debate (Lang and Backer, 2001; Boiron *et al*., 2001; Hart *et al*., 2002; Bouchot
552 *et al*., 2005; Hart, 2007; Zacharias *et al*., 2014; Marcoux *et al*., 2015). In the Bonnac area, the
553 magmatic origin of the fluid is not fully demonstrated by the existing fluid inclusion study (Bril,
554 1982) as they rather display a metamorphic origin (low salinity, complex chemistry enriched in
555 CO_2). However, a magmatic fluid affinity is pointed out by: i) the presence of magmatic affinity
556 element such as the W and the Bi-Te-Au association (Lang and Backer, 2001; Blevin, 2004)
557 and by ii) the spatial and temporal link with leucogranitic dykes. In addition, the lead isotopic
558 compositions measured for different mineralized veins and main lithological formations of the
559 Brioude-Massiac area support such magmatic origin of the metals (Marcoux and Bril, 1986).
560 The $^{207}Pb/^{206}Pb$ ratios estimated on our dating are close to those obtained on the aplitic dykes
561 of leucogranitic composition of the la Margeride granite (see part 6 for the data).

562 To take into account all those features, we propose a genetic link between those mineralized
563 veins and the leucogranitic dykes, where the initial magmatic fluids were derived from the
564 crystallization of an underlying granitic pluton. The heat source supplied by the pluton was
565 responsible for fluid migration toward the high permeability zones. The high temperature (400-
566 500 °C) interaction between the fluid and the host-rocks (greisen type alteration in the vein
567 hanging walls) could have re-equilibrated the fluid, overprinting its initial magmatic signature
568 Then fault-valve mechanisms channeled the ore-fluids into structural discontinuities (Sibson *et*
569 *al*., 1988), and fluid overpressure associated with potential fault-valve mechanism could be
570 responsible for vein opening and the gold-stage 3 deposition, in a shallow crustal environment.

571

572 The chemical composition of the Brioude-Massiac andalusite-leucogranitic S-type magma
573 dykes (EDM 1) is characterized by an oxidizing redox state (Fig. 18), although a reduce redox
574 state is more commonly observed. These characteristics are considered as more favorable than
575 a reduce redox state to form a tungsten ore deposit. Indeed the early magnetite precipitation
576 allows the preservation of Au in the melt fraction of granitic magmas (Blevin, 2004).

577

578 7.5 A new ore deposit model for the Bonnac deposits?

579

580 Because of the metamorphic origin of fluids, the Bonnac deposits was previously classified as
581 an orogenic gold deposit (Bouchot *et al*., 2005), although they do not fulfil all the necessary
582 criteria (Groves *et al*., 1998).
583 The Bonnac deposits share some of the characteristics of the IRGD type (Thompson *et al*.,
584 1999; Lang and Baker, 2001; Hart *et al*., 2002; Gloaguen, 2006; Hart, 2007; Zacharias *et al*.,
585 2014; Marcoux *et al*., 2015) such as: i) the spatial and temporal relationships between ore-

deposition and peraluminous granite emplacement, ii) the peculiar relation between magmatic-source-related ore phases such as bismuth, tellurides, wolframite, löllingite or molybdenite, iii) the contemporaneous bismuth-telluride-gold deposition, iv) the vein deposition during the syn-orogenic extensional period. The redox state of the leucogranitic dykes that spans the boundary of the ilmenite series (Fig. 18) is also a favorable context for IRGD deposits (Lang and Backer, 2001; Blevin, 2004).

On the other hand, the structural evolution from a ductile/brittle deformation to a brittle one, fault-valve mechanism features, and the presence of a late meteoric fluid input, are classical features found for the orogenic gold type deposits (Boiron *et al*., 1990, 2003; Groves *et al*., 1998; Bouchot *et al*., 2005).

Therefore, the Bonnac ore-zone represents a mineralization type intermediate between the orogenic-gold and IRGD models as already demonstrated for the Mokrsko gold deposit in the Bohemian-Massif for example (Zacharias et al., 2014).

8. Conclusions

The Bonnac veins show a W-As-Bi-Au paragenesis that results from polyphase hydrothermal and magmatic events. Three stages of ore deposition have been identified starting with wolframite and löllingite in a deep-seated setting, between 12 to 9 km and up to 400 °C. The second ductile/brittle deformation stage was responsible for scheelite and arsenopyrite deposition at 480-300 °C. The late stage was marked by brittle micro-fracturing infilled with native bismuth, bismuthinite, hedleyite, electrum, pyrite and Cu-Zn-Pb minerals at 266 to 240 °C and 7 to <5 km depth. This could be the result of fault-valve mechanism. The decrease of the temperature-pressure and the sulfide activity caused by ongoing sulfide precipitation seems to be the major factors responsible for the gold deposition during the late stage of deposition.

The mineralized veins are spatially and temporally linked to the emplacement of the andalusite-leucogranitic dykes of the Brioude-Massiac district around 329-315 Ma. Our new LA-ICP-MS U/Pb dating on hydrothermal apatite from the deposit documents an emplacement age around 320 Ma. This genetic link suggests a magmatic-to-hydrothermal transition for the Bonnac ore-forming process. In the newly proposed model, the cooling of a peraluminous pluton might have supplied magmatic fluids, and heat source for mineralized fluid flows toward high permeability zones such as previous discontinuities. The magmatic origin of the fluid has been partly overprinted by fluid-rocks interaction.

The emplacement of both the andalusite-leucogranitic dykes and quartz veins was controlled at the regional scale by a NW-SE extensional direction, consistent with the tectono-magmatic D4 event corresponding to the syn-orogenic extension in the FMC Variscan orogen. This geodynamic event is older than the "Or 300" one, suggesting therefore an earlier fertile metallogenic period at ca. 320 Ma for tungsten and gold deposition in the FMC.

The genetic classification of the Bonnac mineralization is equivocal. The W-As-Bi-Au-quartz veins exhibit the features of both orogenic gold (relatively deep level of emplacement) and IRGD model (spatial-temporal link between the mineralization and the peraluminous intrusion). We propose that it represents an intermediate type between the typical orogenic-gold and IRGD model.

The Serpukhovian to Bashkirian peraluminous andalusite-leucogranitic dyke swarms appear as a favorable metallotect for future mining exploration in the FMC. The widespread occurrences related to this type of magmatism in the FMC suggest that other Bonnac-like, or IRGD-like, deposits probably exist. IRGD deposits, and the economic high-grade gold content in tungsten vein-type, might have been underestimated in the FMC.

Acknowledgements.

This work was funded by e-Mines Company through its R&D activity, and the ISTO with contribution from ANRT. The authors thank the following persons for their technical support and valuable advices: T. Poitrenaud, B. Cochelin, A. Beaudoin, R. Augier, C. Montmartin J. Gouin, M. Picault. We particularly thank I. Di-Carlo (ISTO) for the SEM, cathodoluminescence and microprobe analyses and for valuable advices. S. Janiec, G. Badin, and P. Benoist-Julliot (ISTO) for thin sections preparation, and technical assistance, and the GeOHeLiS platform for the LA-ICP-MS dating.

References

Audion AS, Labbé JF. 2012. Panorama mondial 2011 du marché du tungstène. Rapport Public BRGM, RP-61341-FR 108p.

Barton P.B, Skinner B.J. 1979. Sulfide mineral stabilities. In: Barnes, H.L. (Ed.), Geochemistry of Hydrothermal ore Deposits. John Wiley, New York, pp. 278–403.

Bernard-Griffiths J, Lasnier B, Marchand J, Vidal P. 1980. Approche par la méthode Rb/Sr de l'étude de granulites acides en Haut-Allier (Massif Central français). *Réun Ann Sci Terre* 8 : 41 p.

Béziat P, Prouhet JP, Tollon F. 1980. Le district de Montredon-Labessonnié (Tarn): W, Sn, F. Publications du 26e Congrès Géologique International (Paris): Gisements français 7, 42 p.

Bogdanoff S, Cirodde JL, Ploquin A, Ramboz C, Le Chapelain JR, Mignon R. 1987. Exploration for tungsten in the Châtaigneraie district. *Chron Rech Min* 487: 11–30.

Blevin P.L. 2004. Redox and compositional parameters for interpreting the granitoid metallogeny of eastern Australia: Implications for gold-rich ore systems: *Resource Geology* 54: 241–252.

Boiron M.C, Cathelineau M, Dubessy J, Bastoul A.M. 1990. Fluids in Hercynian Au veins of from the French Variscan belt. *Mineralogical Magazine* 54: 231–243.

Boiron M.C, Barakat A, Cathelineau M, Banks D.A, Durisova J, Moravek P. 2001. Geometry and P-V-T-X conditions of microfissural ore fluid migration: the Mokrsko gold deposit (Bohemia). *Chem Geol* 173: 207-225.

Boiron M-C, Cathelineau M, Banks DA, Fourcade S, Vallance J. 2003. Mixing of metamorphic and surficial fluids during the uplift of the Hercynian upper crust: consequences for gold deposition. *Chem Geol* 194: 119–141.

Bouchot V, Ledru P, Lerouge C, Lescuyer J-L, Milesi J-P. 2005. Late Variscan mineralizing systems related to orogenic processes: the French Massif Central. *Ore Geol Rev* 27: 169–197.

Bril H. 1982. Fluid inclusions study of Sn-W-Au, Sb- and Pb-Zn mineralizations from the Brioude-Massiac district (French Massif Central). *Tschermaks Min Petr Mitt* 30: 1-16.

Bril H. 1983. Etude métallogénique des minéralisations à antimoine et associées du district de Brioude-Massiac (Massif Central français) ; conditions géochimiques de dépôt, implications génétiques, PhD thesis : Université Clermond-Ferrand, 341pp.

Bril H, Beaufort D. 1989. Hydrothermal alteration and fluid circulation related to W, Au, and Sb vein mineralizations, Haut-Allier, Massif Central, France: *Econ Geol* 84: 2237–2251.

Bril H, Bonhomme M.G, Marcoux E, Baubron J.C. 1991. Ages K/Ar des minéralisations de Brioude-Massiac (W-Au-As-Sb; Pb-Zn), Pontgibaud (Pb-Ag; Sn), et Labessette (As-Pb-Sb-Au): Place de ces districts dans l'évolution géotectonique du Massif Central français: *Miner Deposita* 26: 189-198.

Burg J-P, Matte P. 1978. A cross section through the French Massif Central and the scope of its Variscan geodynamic evolution. Z. dt. Geol. Ges. 129 : 429-460.

Chantraine J, Autran A, Cavelier C. 1996. Geological map of France, 1/1 000 000. BRGM, Orléans.

Charonnat X. 2000. Les minéralisations aurifères tardi-hercyniennes des Cévennes, PhD thesis, Université d'Orléans, 1 Vol, 259 pp.

Chauvet A, Volland-Tuduri N, Lerouge C, *et al*. 2012. Geochronological and geochemical characterization of magmatic-hydrothermal events within the Southern Variscan external domain (Cévennes area, France). *Int J Earth Sci.* 101: 69-86.

Cheval-Garabédian F. 2019. Les minéralisations à Sb et Au tardi-varisques : vers un modèle génétique unifié ? Exemples du Massif armoricain et du Massif central, PhD thesis, Université d'Orléans, 1 Vol, 498pp.

Cheval-Garabédian F, Faure M, Marcoux E, Gouin J, Picault M. 2020. The La Bellière gold and antimony district (French Armorican Massif): A two-stage evolution model controlled by Variscan strike-slip tectonic. *Ore Geol Rev* 125: 103–681.

Chew D.M, Petrus J.A, Kamber B.S. 2014. U-Pb LA–ICPMS dating using accessory mineral standards with variable common Pb. *Chem Geol* 363: 185–199.

Ciobanu C.L, Cook N.J, Damian F, Damian G. 2006. Gold scavenged by bismuth melts: an example from Alpine shear-remobilizations in the Highis Massif Romania. *Mineral Petrol* 87: 351–384.

Ciobanu C L, Birch W D, Cook N J, Pring A, Grundler P. V. 2010. Petrogenetic significance of Au–Bi–Te–S associations: the example of Maldon, Central Victorian gold province, Australia. *Lithos* 116: 1-17.

Cook N.J, Ciobanu C.L, Wagner T, Stanley C.J. 2007. Minerals of the system Bi–Te–Se–S related to the tetradymite archetype: review of classification and compositional variation. *Can Mineral* 45: 665–708.

Cox S.F. 1987. Antitaxial crack-seal vein microstructures and their relationships to displacement paths. *J Struct Geol* 9: 79–787.

Cox S.F, Wall V.J, Etheridge M.A, Potter T.F. 1991. Deformation and metamorphic processes in the formation of mesothermal vein-hosted gold deposits, examples from the Lachlan Fold Belt in central Victoria Australia. *Ore Geol Rev* 6: 391–423.

Cuney M, Alexandrov P, Le Carlier de Veslud C, *et al*. 2002. The timing of W Sn rare metals mineral deposit formation in the Western Variscan chain in their orogenic setting: the case of the Limousin area (Massif Central, France). In: Blundell, D.J., Neubauer, F.,von Quadt, A. (Eds.), The Timing and Location of Major Ore Deposits in an Evolving Orogen, *Geological Society, London*, Special Publications 204: 213–228.

716 Debon F, Le Fort P. 1988. A cationic classification of common plutonic rocks and their
717 magmatic associations: principles, method, applications. *Bulletin de Minéralogie* 111 :
718 493-510.
719 De Gramont X, Feybesse J.L, Lambert A. 1990. Synthèse du district de Brioude-Massiac et des
720 confins nord de la Margeride (Massif Central). Rapp BRGM DAM/DL/C/ R-30695. 191
721 p.
722 Delvaux D, Sperner B. 2003. Stress tensor inversion from fault kinematic indicators and focal
723 mechanism data: the TENSOR program. *New insights into structural interpretation and*
724 *modelling*, 212: 75-100.
725 Demange M, Nicolas V-A, Soler P, Giouse H. 1988. Le gisement tungstifère de Leucamp
726 (Cantal, France). Contrôles géologiques et minéralisations. *Bull. Soc. Géol. France*, 4 :
727 559-570.
728 Derré C. 1983. La province à Sn-W ouest-européenne. Histoire de divers types de gisements
729 du Massif Central, des Pyrénées et du Portugal. Distributions des gisements, PhD thesis:
730 Université Paris VI, 2 vol., I, 345p., II, 421p.
731 Dimitrova D, Kerestedjian T. 2006. Bismuth minerals in the postskarn sulphide-arsenide
732 mineralization in the Martinovo iron deposit, NW Bulgaria: Geochemistry, Mineralogy and
733 Petrology, Sofia, v. 44, 19-32.
734 Faure M. 1995. Late orogenic carboniferous extensions in the Variscan French Massif Central.
735 *Tectonics* 14: 132–153.
736 Faure M, Pons J. 1991. Crustal thinning recorded by the shape of the Namurian-Westphalian
737 leucogranites in the Variscan belt of the Northwest Massif Central, France. *Geology* 19:
738 730-733.
739 Faure M, Be Mézème E, Duguet M, Cartier C, Talbot J-Y. 2005. Paleozoic tectonic evolution
740 of medio-Europa from the example of the French Massif Central and Massif Armorican.
741 In: (eds.) Carosi, R., Dias, R., Iacopini, D., and Rosenbaum, G., The southern Variscan
742 belt, *Journal of the Virtual Explorer*, Electronic Edition, ISSN 19: 1441–8142.
743 Faure M, Lardeaux J.-M, Ledru P. 2009. A review of the pre-Permian geology of the Variscan
744 French Massif central. *Comptes Rendus Geoscience* 341 : 202-213.
745 Gaboury D, Daigneault R. 2000. Flat vein formation in a transitional crustal setting by self-
746 induced fluid pressure equilibrium, an example from the Géant Dormant gold mine Canada.
747 *Ore Geol Rev* 17: 155-178.
748 Gloaguen E. 2006. Apport d'une étude intégrée sur les relations entre granite et minéralisations
749 filoniennes (Au et Sn-W) en contexte tardi-orogénique, PhD thesis: Université d'Orléans.
750 Groves D.I, Goldfar, R.J, Gebre-Mariam M, Hagemann S.G, Robert F. 1998. Orogenic gold
751 deposits, a proposed classification in the context of their crustal distribution and
752 relationship to other gold deposit types. *Ore Geol Rev* 13: 7–27.
753 Harlaux M, Marignac C, Cuney M, Mercadier J, Magott R, Mouthier B. 2015. Nb-Ti-Y-HREE-
754 WU oxide minerals with uncommon compositions associated with the tungsten
755 mineralization in the Puy-les-Vignes deposit (Massif central, France): Evidence for rare-
756 metal mobilization by late hydrothermal fluids with a peralkaline signature. *Can Mineral*
757 53: 653-672.
758 Harlaux M, Romer R. L, Mercadier J, Morlot C, Marignac C, Cuney M. 2018. 40 Ma of
759 hydrothermal W mineralization during the Variscan orogenic evolution of the French
760 Massif Central revealed by U-Pb dating of wolframite. *Miner Deposita* 53: 21-51.
761 Hart C.J.R, McCoy D, Goldfarb R.J, *et al*. 2002. Geology, exploration and discovery of the
762 Tintina gold province, Alaska and Yukon. Society of economic geologists special
763 publication 9: 241-274.

764 Hart C. J. 2007. Reduced intrusion-related gold systems. Geological Association of Canada,
765 Mineral Deposits Division, 5: 95-112.
766 Joly A, Chen Y, Faure M, Martelet G. 2007. multidisciplinary study of a syntectonic pluton
767 close to a major lithospheric-scale fault: relationships between the Montmarault granitic
768 massif and the Sillon Houiller Fault in the Variscan French Massif Central. Part I:
769 Geochronology, mineral fabrics and tectonic implications, *J Geophys Res*: 112, B10104,.
770 Joly A., Faure M, Chen Y, Martelet G. 2009. Gravity inversion, AMS and geochronological
771 investigations of syntectonic granitic plutons in the southern part of the Variscan French
772 Massif Central. *J. Struct. Geol.*, 31: 421-443.
773 Kretschmar U, Scott S.D. 1976. Phase relations involving arsenopyrite in the system Fe-As-S
774 and their application: *Can Mineral* 14: 364–386.
775 Lang J-R, Baker T. 2001. Intrusion related gold systems: the present level of understanding.
776 *Miner Deposita* 36: 477–489.
777 Lasnier B. 1977. Persistance d'une série granulitique au cœur du Massif central français (Haut
778 Allier). Les termes basiques, ultrabasiques et carbonatés. PhD. Thesis, Université de
779 Nantes, 341pp.
780 Lasnier B, Marchand J, Bouilkler R, Burg J-P, Cornen G, Forestier F.H Leyreloup A. 1982.
781 Notice de la carte géologique de France (1/50 000), feuille de Brioude (766) – BRGM,
782 Orléans.
783 Ledru P, Lardeaux J. M, Santallier D A, *et al*. 1989. Où sont les nappes dans le Massif central
784 français ? *Bulletin de la Société géologique de France* 3 : 605-618.
785 Lerouge C, Bouchot V .2009. Conditions of formation and origin of fluids of quartz-tourmaline
786 veins in the La Châtaigneraie tungstiferous district (Massif Central, France): fluid inclusions
787 and stable isotopes. *B Soc Geol Fr* 180: 263-270.
788 Linnen RL, Cuney M. 2005. Granite-related rare-element deposits and experimental
789 constraints on Ta-Nb-W-Sn-Zr-Hf mineralization. In: Rare-element geochemistry and
790 mineral deposits (eds. R.L. Linnen and I.M. Samson). *Geological Association of Canada,*
791 *GAC Short Course* Notes 17: 45 – 68.
792 Malavieille, J., P. Guihot, S. Costa, J.M. Lardeaux, and V. Gardien, 1990. Collapse of the
793 thickened Variscan crust in the French Massif Central: Mont Pilat extensional shear zone
794 and St.-Etienne Late Carboniferous basin. *Tectonophysics* 177: 139-149.
795 Marchand J. 1974. Persistance d'une série granulitique au cœur du Massif central français
796 (Haut Allier). Les termes acides. PhD. Thesis, Université de Nantes, 267pp.
797 Marcoux E, Picot P. 1985. Les minéralisations de Pontgibaud (Puy-de-Dôme): Une approche
798 complémentaire par géochimie isotopique du plomb et les paragenèses. *Chronique de la*
799 *Recherche Minière* 481 : 27-38.
800 Marcoux E, Bril H. 1986. Héritage et sources de métaux d'après la géochimie isotopique du
801 plomb ; Etude des minéralisations filoniennes du Haut-Allier (Massif Central, France).
802 *Miner Deposita* 21 : 35-43.
803 Marcoux E, Bonnemaison M. 1988. La géochimie isotopique du plomb et la prospection de l'or
804 en France. In: Johan Z, newstetter D (eds) Gisements métallifères dans leur contexte
805 géologique. Doc BRGM 158: 489–508.
806 Marcoux E, Nerci K, Branquet Y, *et al*. 2015. Late-Hercynian Intrusion-related gold deposits:
807 an integrated model on the Tighza polymetallic district, central Morocco. *Journal of African*
808 *Earth Sciences* 107: 65-88.
809 Marignac C, Cuney M (1999) Ore deposits of the French Massif Central: insight into the
810 metallogenesis of the Variscan collision belt. *Miner Deposita* 34: 472 – 504.

Mathonnat M. 1983. La série métamorphique du Cézallier, Massif central français, PhD thesis: Université de Clermont-Ferrand.
McDowell F.W, McIntosh W.C, Farley K.A. 2005. A precise 40Ar–39Ar reference age for the Durango apatite (U–Th)/He and fission-track dating standard. *Chem Geol* 214: 249–263.
Monié P, Bouchot V, Faure M, Charonnat X, Najoui K. 1999. 40Ar/39Ar Laser-Probe Dating of W, Au and/or Sb Deposits and associated granites in the Southern French Massif Central (Cévennes, Châtaigneraie), EUG 10, abstract volume, Strasbourg, Terra Abstracts, p 477.
Monié P, Respaut J.-P, Brichaud S, Bouchot V, Faure M, Roig J.-Y. 2000. 40Ar/39Ar and U–Pb geochronology applied to Au–W–Sb metallogenesis in the Cévennes and Châtaigneraie districts (Southern Massif Central, France). In: Bouchot, V., Moritz, R. (Eds.), A Geode–GéoFrance 3D Workshop on Orogenic Gold Deposits in Europe with Emphasis on the Variscides; Extended Abstracts. Documents du BRGM, 297 : 77–79.
Morisson G W, Rose W J, Jaireth S. 1991. Geological and geochemical controls on the silver content (fineness) of gold in gold-silver deposits. *Ore Geol Rev* 6: 333–364.
Nicaud J. 2001. Contrôle structural de la mise en place des minéralisations aurifères du district de Saint-Yrieix : analyse de la fracturation, étude des altérations hydrothermales, PhD thesis: Université de Limoges. 252p.
Paquette J.L, Piro J.L, *et al*. 2014. Sensitivity enhancement in LA-ICP-MS by N2 addition to carrier gas: Application to radiometric dating of U-Th-bearing minerals. *Agilent ICP-MS J* 58: 4–5.
Paton C, Woodhead J.D, Hellstrom J.C, Hergt J.M, Greig A, Maas R. 2010. Improved laser ablation U-Pb zircon geochronology through robust downhole fractionation correction. *Geochem. Geophys. Geosyst*. 11 Q0AA06.
Périchaud J.J. 1970. Les gisements métalliques du district d'antimoine de Brioude-Massiac (Massif central français), PhD thesis: Université de Clermont Ferrand. 771 p.
Pin C, Peucat J-J. 1986. Ages des épisodes de métamorphisme paléozoïques dans le Massif central et le Massif armoricain. Bull. Soc. Géol. France, 8, t. II, n°3, 461–469.
Pochon A, Gapais D, Gloaguen E, *et al*. 2016. Antimony deposits in the Variscan Armorican belt, a link with mafic intrusives? *Terra Nova* 28: 138-145. doi: 10.1111/ter.12201.
Poitrenaud T, Poujol M, Augier R, Marcoux E. 2019. The polyphase evolution of a late Variscan W/Au deposit (Salau, French Pyrenees): insights from REE and U/Pb LA-ICP-MS analyses. *Miner Deposita*: 1-21.
Ramsay J.G. 1980. The crack-seal mechanism of rock deformation. *Nature* 284: 135–139.
Robert F, Boullier A.M, Firdaous K. 1995. Gold–quartz veins in metamorphic terranes and their bearing on the role of fluids in faulting. J. Geophys. Res. 100: 12841-12859.
Romer RL, Kroner U. 2016. Phanerozoic tin and tungsten mineralization–tectonic controls on the distribution of enriched protoliths and heat sources for crustal melting. *Gondwana Res* 31: 60 – 95.
Sandras A. 1988. Les structures auro-antimonifères du district de Brioude–Massiac. Gîtologie et métallogénie des concentrations aurifères, PhD thesis: Université de Nancy. 211 p.
Scaillet S, Cheilletz A, Cuney M, Farrar E, Archibald DA. 1996. Cooling pattern and mineralization history of the saint Sylvestre and western Marche leucogranite pluton, French massif central: I.40Ar/39Ar isotopic constraints. *Geochim Cosmochim Acta* 60: 4653 – 4671.
Schoene B, Bowring S.A. 2006. U-Pb systematics of the McClure Mountain syenite: thermochronological constraints on the age of the 40Ar/39Ar standard MMhb. *Contrib. Mineral Petrol* 151: 615–630.
Scholz C. H. 1988. The brittle-plastic transition and the depth of seismic faulting. *Geologische Rundschau* 77: 319-328.

Sibson R.H, Robert F, Poulsen K.H. 1988. High-angle reverse faults, fluid pressure cycling, and mesothermal gold–quartz deposits. *Geology* 16: 551–555.

Sharp Z. D, Essene E. J, Kelly W. C. 1985. A re-examination of the arsenopyrite geothermometer; pressure considerations and applications to natural assemblages. *Can. Mineral*. 23: 517-534.

Stipp M, Stünitz H, Heilbronner R, Schmid S.M. 2002. The eastern Tonale fault zone: a natural laboratory for crystal plastic deformation of quartz over a temperature range from 250 to 700 °C. *Journal of Structural Geology* 24: 1861–1884.

Talbot J. Y. Faure M, Chen Y, Martelet G. 2005a. Pull-apart emplacement of the Margeride granitic complex (French Massif Central). Implications for the late evolution of the Variscan orogen. *Journal of Structural Geology*, 27: 1610-1629.

Talbot JY, Chen Y, Faure M. 2005b. Pluton-dykes relationships from AMS and microstuctural studies in a Variscan granite from French Massif Central, *J Geophys Res* 110.

Thompson J.F.H, Sillitoe R.H, Baker T, Lang J.R, Mortensen J.K. 1999. Intrusion related gold deposits associated with tungsten–tin provinces. *Miner Deposita* 34: 323–334.

Thomson S.N, Gehrels G.E, Ruiz J, Buchwaldt R. 2012. Routine low-damage apatite U-Pb dating using laser ablation–multicollector–ICPMS. *Geochem Geophys Geosyst* 13: Q0AA21.

Thonat A, Mathonnat M, Pin C, Rocher P, Bertin C, Chèvremont P. 2014. Notice de la carte géologique de France au 1/50 000°, 765, Massiac. 141p.

Vermeesch, P., 2018. IsoplotR: A free and open toolbox for geochronology. *Geosci. Front*. 9, 1479–1493. https://doi.org/10.1016/J.GSF.2018.04.001

Williams-Jones A. E, Bowell R. J, Migdisov A. A. 2009. Gold in solution. *Elements* 5: 281-287.

Wood, S.A. Samson, I.M. 2000. The Hydrothermal Geochemistry of Tungsten in Granitoid Environments: I. Relative Solubilities of Ferberite and Scheelite as a Function of T, P, pH, and mNaCl. *Econ Geol* 95: 143-182.

Zachariáš J, Moravek P, Gadas P, Pertoldova J. 2014. The Mokrsko-West gold deposit, Bohemian Massif, Czech Republic: mineralogy, deposit setting and classification. *Ore Geol Rev* 58: 238-263.

Figures captions

Fig. 1. Geological map of the French Massif Central (modified from Faure *et al.,* 2009), with the location of, the tungsten deposits and occurrences (from Audion and Labbé, 2012), and the study area. Tungsten district name abbreviations: ECH: Echassières; ENG: Enguialès; FUM: Fumade; GOU: St-Goussaud; LCP: Leucamp; MAN: Mandelesse; ML: Montredon-Labessonnière; NF: Neuf-Jours; PLV: Puy-les-Vignes; SM: St-Mélany; VAU: Vaulry.

Fig. 2. Location of the study area within the geological and metallogenic framework of the Brioude-Massiac district. The simplified geology modified from Lasnier *et al.* (1982) and Thonat *et al.* (2014). Location and extension of mineralized veins are from Périchaud, (1970).

Fig. 3. Geological and structural map of the Bonnac area with the location of most interesting outcrops.

Fig. 4. A) Representative arsenopyrite (Asp) and wolframite (Wolf) bearing quartz vein from the Costillon vein (outcrop A in Fig.3) showing the structural features and the relationships with the paragneiss host-rock and the leucogranitic dykes. B) Detail of drag folds developed in the country-rock paragneiss along the contact between the arsenopyrite (Asp) and wolframite (Wolf) bearing quartz veins and leucogranitic dyke. La Borie vein (outcrops B in Fig.3).

Fig. 5. A) Detail picture of the Fig.4B W-As-Bi-Au bearing quartz vein crosscutting leucogranitic dykes, (La Borie vein, outcrops B in Fig.3). B) Fault plane seen on Fig. 5A with high angle pitch striation. C) Cm-sized mineralized quartz veins network crosscutting the leucogranitic dyke (the Rode vein, outcrops C on Fig.3). D) Focus on the fault plane in the mineralized vein of the figure 5C showing a normal kinematics.

Fig. 6. Mine gallery opened in the Ferbert vein. A) Low angle wolframite (Wolf) and arsenopyrite (Asp)-bearing quartz vein (outcrops D in Fig.3). The vein is cut by late sub-vertical barren fault. B) Detail of the quartz vein showing normal kinematics.

Fig. 7. A) 3D block showing the main structural observations made on the mineralized quartz veins from Bonnac area. They allow us to propose a relative chronology of the structures developed in the paragneissic host-rock, the leucogranitic dykes and the quartz veins. B) Stereogram (lower hemisphere projection) of the poles of the fault planes coeval with the emplacement of the mineralized veins, leucogranitic dykes, and late faults measured in the field.

Fig. 8. Representative W-As-Bi-Au-bearing quartz hand sample from the Androl vein (see Fig.3 for localization), with arsenopyrite, wolframite, scheelite, and muscovite. Sample is observed in natural light (left) and UV light (254 nm, right).

Fig. 9. Microphotographs showing the mineralogy of the stages 1 and 2 at Bonnac. A) Coarse wolframite (Wolf) with lollingite (Lo) fractured and cemented by rhombic arsenopyrite (Asp). Secondary scheelite (Sch) pseudomorphs after wolframite. Arsenopyrite is fractured and cemented by bismuthinite (Bit), (Androl vein). B) Cathodoluminescence view showing the relationships between lollingite (Lo), weakly deformed macrocristalline quartz (Qz1), and arsenopyrite (Asp) rhombic crystals cutting Qz1, (Costillon vein). C) Wolframite (Wolf) and

coarse hydrothermal apatite (Ap) assemblage fractured and cemented by secondary scheelite (Sch) and minor pyrite (Py), (Ferbert vein). D) Highly sheared macrocristalline quartz (Qz1) crosscut by a second quartz generation (Qz2), (see text for further explanation). Relics of Qz1 clasts are present in the upper right part of the photograph, (Ferbert vein).

Fig. 10. Microphotographs showing the mineralogy of stage 3. A) Macrocristalline quartz (Qz1) and highly sheared quartz (Qz2) crosscut by microcracks with fluid inclusions and bismuth minerals (Bi minerals), (Ferbert vein). B) Relationships of sheared quartz (Qz1) with neoformed quartz (Qz2), crosscut by microcracks with bismuthinite (Bit) and electrum (El), (Ferbert vein. C) Lollingite aggregates (Lo) highly fractured and cemented by hyaline quartz (Qz3) with bismuthinite (Bit), (La-Rode vein. D) Same picture as C) in transmitted, polarized light. E) Lollingite (Lo) crosscut by an assemblage of native bismuth (Bi) and bismuthinite (Bit), (Androl vein). F) back scattered electron image of the complex Bi-Te assemblage formed in stage 3. Native rounded shape bismuth (Bi) with bismuthinite (Bit) and tetrahedrite (Ttr), horobetsuite (Hor) in a hedleyite (Hed) crystal. Ox: unknown oxydes, (Ferbert vein).

Fig. 11. Microphotographs showing gold habits of stage 3 at Bonnac. A) Lollingite (Lo) with inclusions of electrum (El) within a native bismuth (Bi) - bismuthinite (Bit) patch, (Androl vein). B) Fractured wolframite (Wolf) cemented by bismuthinite (Bit), electrum (El), hedleyite (Hed) and native bismuth (Bi), (Ferbert vein). C) Residual lollingite (Lo) fractured and cemented by arsenopyrite (Asp) at its turn fractured and cemented by bismuthinite (Bit), electrum (El), hedleyite (Hed) and native bismuth (Bi), (Ferbert vein). D) Fractured arsenopyrite (Asp) cemented by chalcopyrite (Ccp) with bismuthinite (Bit) inclusions, sphalerite (Sp), electrum (El), (Ferbert vein). E) Fractured arsenopyrite (Asp) cemented by chalcopyrite (Ccp) with bismuthinite (Bit) inclusions, sphalerite (Sp), tetrahedrite (Trt), euhedral pyrite (Py) contemporaneous with euhedral quartz (Qz4), (Ferbert vein).

Fig. 12. Paragenetic succession of the Bonnac W-As-Bi-Au mineralization. See text for details.

Fig. 13. A) and B) cathodoluminescence images of some of the dated apatite grains from Bonnac (A, Androl vein, B, Ferbert vein). C) and D) Tera-Wasserburg concordia diagrams for the hydrothermal apatite from Bonnac. n corresponds to the number of apatite grains analyzed. Ellipses and errors are reported at 2σ.

Fig. 14. Summary of the evolution of the estimated mineral deposition temperatures for the 3 stages of mineralization of the Bonnac veins, based on all available data. Fluids inclusions data are from Bril (1982), estimated temperature for quartz textural deformation are from Stipp *et al.* (2002).

Fig. 15. Stereographic projection of faults planes contemporaneous of mineralized quartz veins with their kinematics and associated striae. σ1, σ2, σ3: orientation of principal stress axe calculated from fault-slip data inversion using WinTensor software in Schmidt's lower hemisphere equal-area projection (Delvaux and Sperner, 2003).

Fig. 16. A) Synthesis of the structural control and radiometric age compilation of orogenic gold ± antimony district, W-Sn and W-Bi-Au vein-type districts (Beziat *et al.*, 1980; Bouchot *et al.*,

2005; Harlaux *et al*., 2018). White boxes correspond to U-Pb dating on wolframite by TIMS method, from Harlaux *et al.* (2018). Black boxes correspond to Ar/Ar dating on muscovite from Monier *et al.* (1999, 2000). For the orogenic-gold deposits, le Châtelet dating (K/Ar on illites) is from Bouchot *et al.* (2005); from Nicaud, (2001) for Saint-Yrieix district (K/Ar on illite); from Chauvet *et al.* (2012) for the Cévennes district (Ar/Ar on muscovite). District name abbreviations are the same as in figure 1. Geological map modified after Chantraine *et al.* (1996). B) The Bonnac hydrothermal event is replaced in the different geodynamic events of the Variscan orogen in the French Massif Central (Faure *et al.*, 2009).

Fig. 17. Metallogenic model of the Bonnac W-Bi-Au quartz veins system (not to scale).

Fig. 18. Fe_2O_3/FeO vs SiO_2 diagram for granitoid rocks associated with various mineral deposits, compiled from Harlaux *et al.* (2018). Data from the leucogranitics dykes of the Brioude-Massiac district are from Sandras, (1988).

Table 1 Summary of the EPMA assays obtained on arsenopyrite from the Brioude-Massiac W-As-Bi-Au veins and gold from Bonnac. Estimated temperatures of crystallization with the arsenopyrite geothermometer are compared with the fluid-inclusions data (Bril, 1982).

Figures

Figure 1

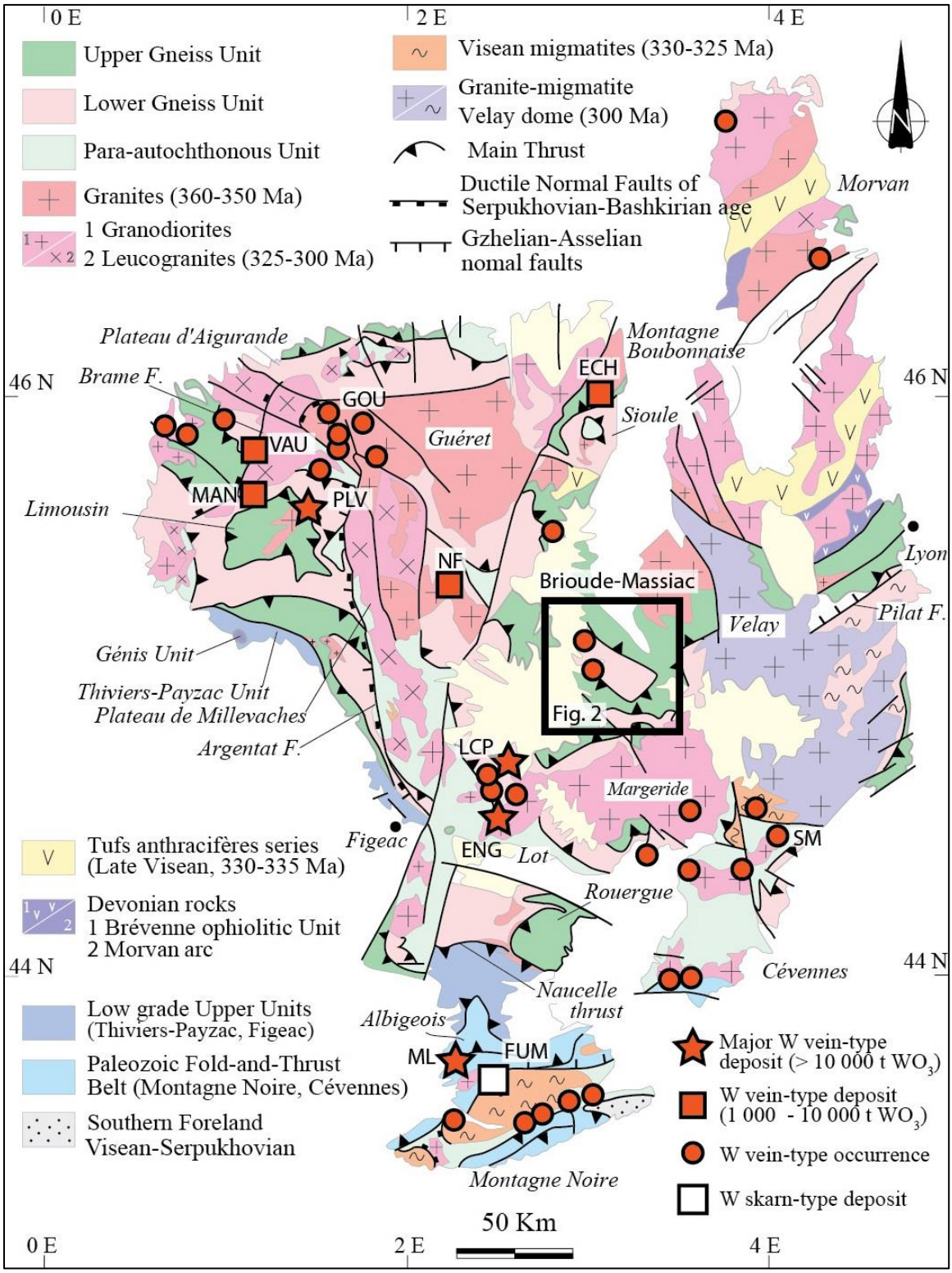

Figure 2

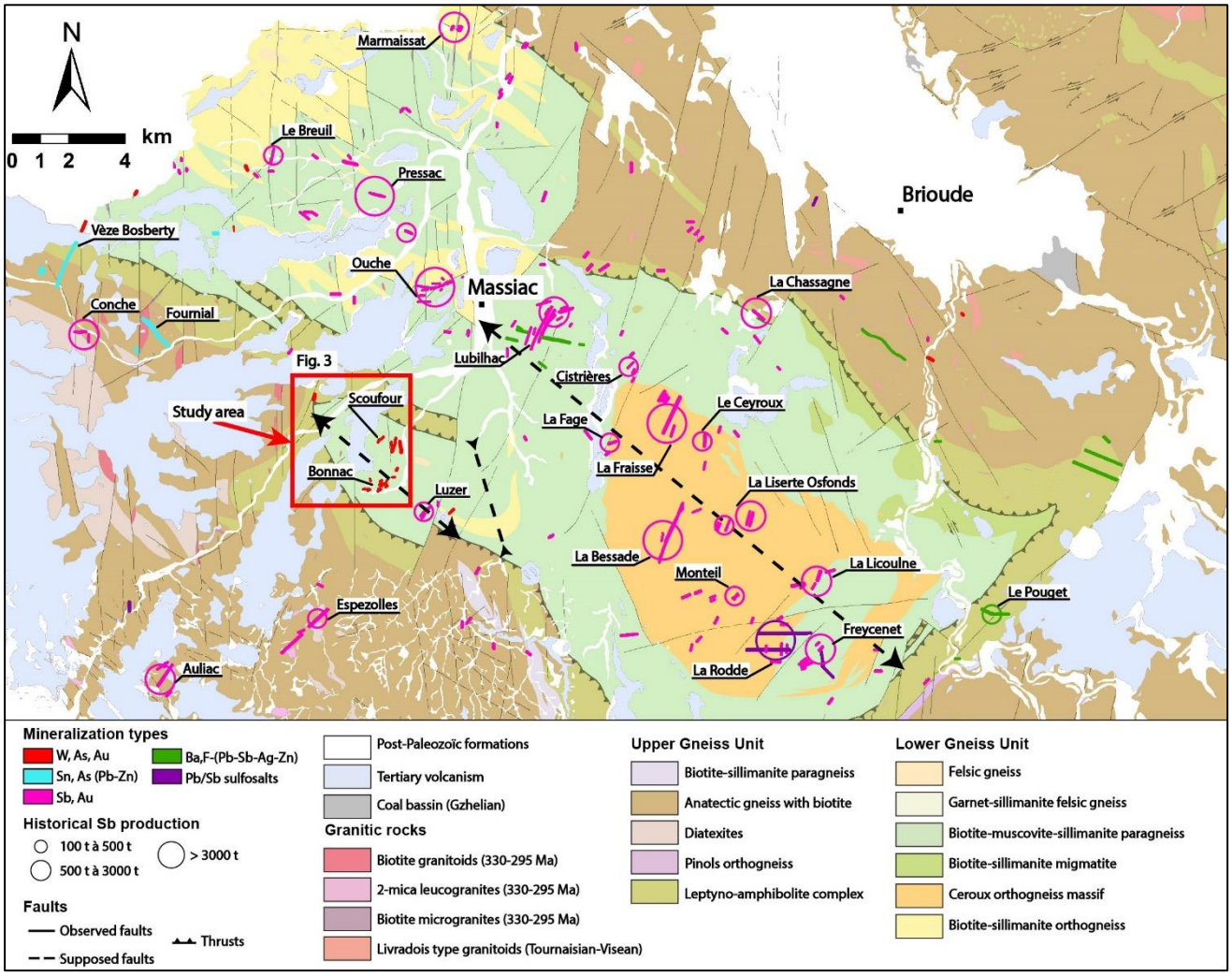
N
km
0 1 2 4
Marmaissat
Le Breuil
Pressac
Brioude
Vèze Bosberty
Ouche
Massiac
La Chassagne
Conche
Fournial
Fig. 3
Lubilhac
Cistrières
Study area
Scoufour
Le Ceyroux
La Fage
Bonnac
La Fraisse
La Liserte Osfonds
Luzer
La Bessade
Monteil
La Licoulne
Le Pouget
Espezolles
Freycenet
Auliac
La Rodde
Mineralization types
W, As, Au
Ba,F-(Pb-Sb-Ag-Zn)
Sn, As (Pb-Zn)
Pb/Sb sulfosalts
Sb, Au
Historical Sb production
100 t à 500 t
> 3000 t
500 t à 3000 t
Faults
Observed faults
Thrusts
Supposed faults
Post-Paleozoïc formations
Tertiary volcanism
Coal bassin (Gzhelian)
Granitic rocks
Biotite granitoids (330-295 Ma)
2-mica leucogranites (330-295 Ma)
Biotite microgranites (330-295 Ma)
Livradois type granitoids (Tournaisian-Visean)
Upper Gneiss Unit
Biotite-sillimanite paragneiss
Anatectic gneiss with biotite
Diatexites
Pinols orthogneiss
Leptyno-amphibolite complex
Lower Gneiss Unit
Felsic gneiss
Garnet-sillimanite felsic gneiss
Biotite-muscovite-sillimanite paragneiss
Biotite-sillimanite migmatite
Ceroux orthogneiss massif
Biotite-sillimanite orthogneiss

Figure 3

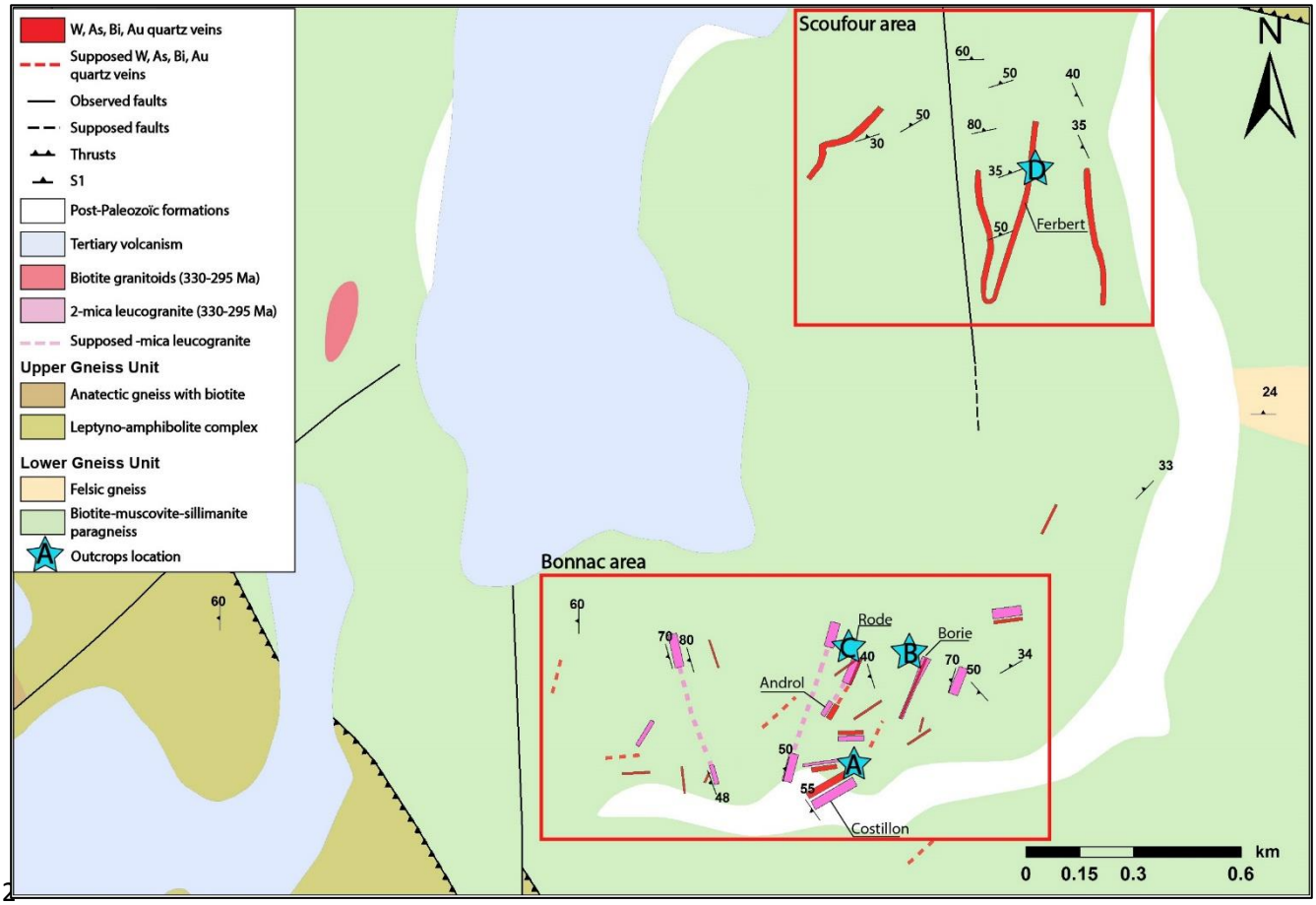
W, As, Bi, Au quartz veins
Supposed W, As, Bi, Au quartz veins
Observed faults
Supposed faults
Thrusts
S1
Post-Paleozoïc formations
Tertiary volcanism
Biotite granitoids (330-295 Ma)
2-mica leucogranite (330-295 Ma)
Supposed -mica leucogranite
Upper Gneiss Unit
Anatectic gneiss with biotite
Leptyno-amphibolite complex
Lower Gneiss Unit
Felsic gneiss
Biotite-muscovite-sillimanite paragneiss
Outcrops location
Scoufour area
Ferbert
Bonnac area
Rode
Borie
Androl
Costillon
N
km
0 0.15 0.3 0.6

Figure 4

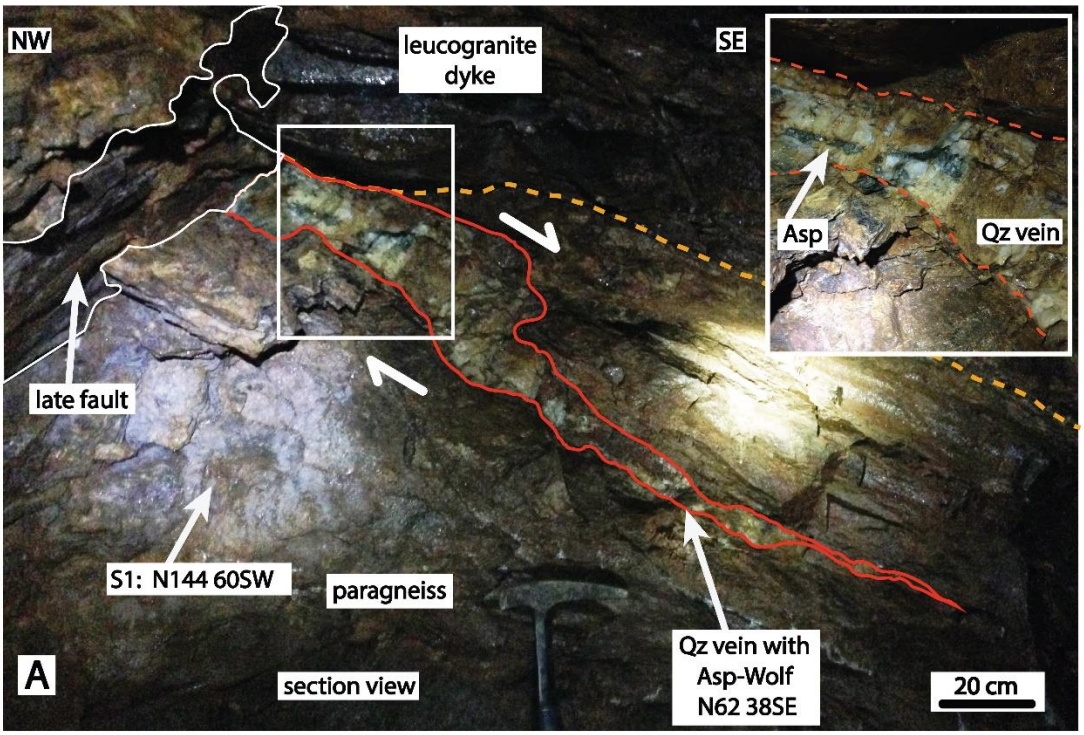
NW
leucogranite dyke
SE
Asp
Qz vein
late fault
S1: N144 60SW
paragneiss
Qz vein with Asp-Wolf N62 38SE
A
section view
20 cm

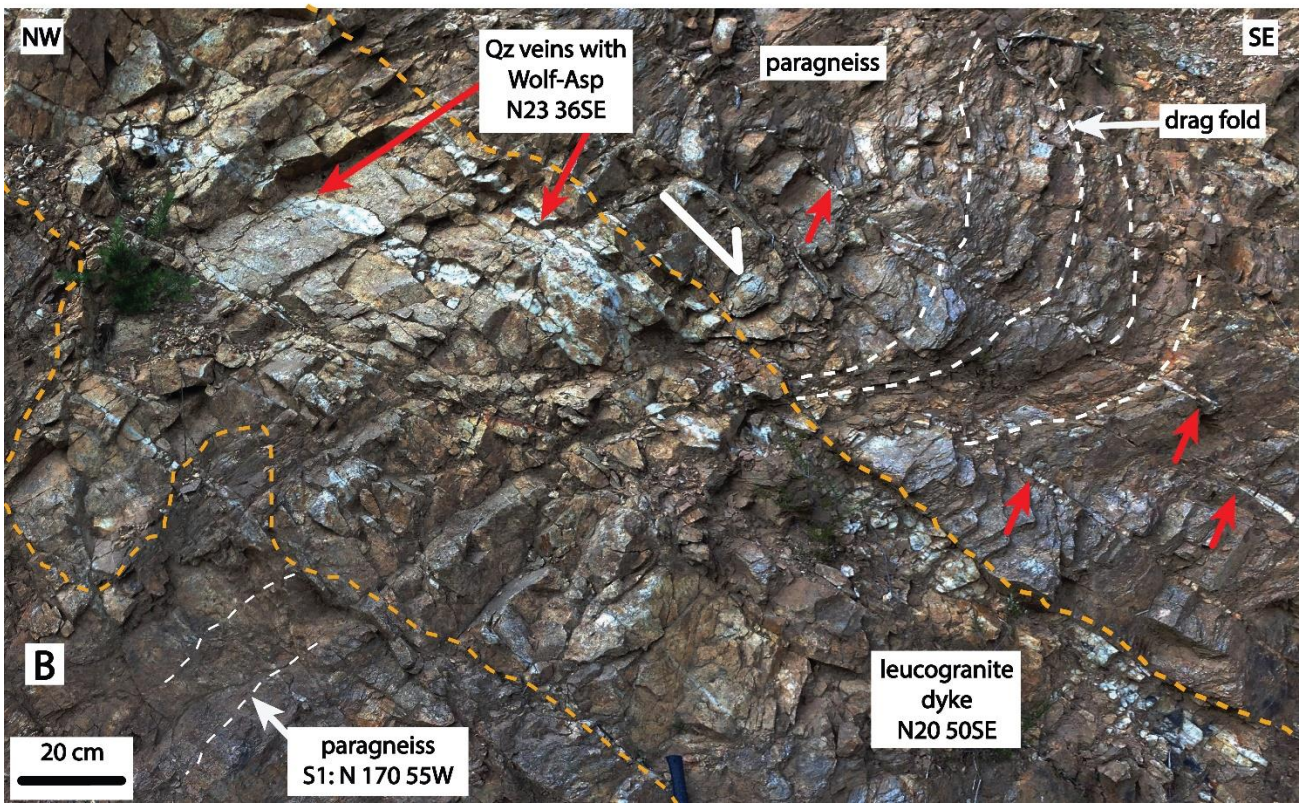
NW
Qz veins with Wolf-Asp N23 36SE
paragneiss
SE
drag fold
B
20 cm
paragneiss S1: N 170 55W
leucogranite dyke N20 50SE

Figure 5

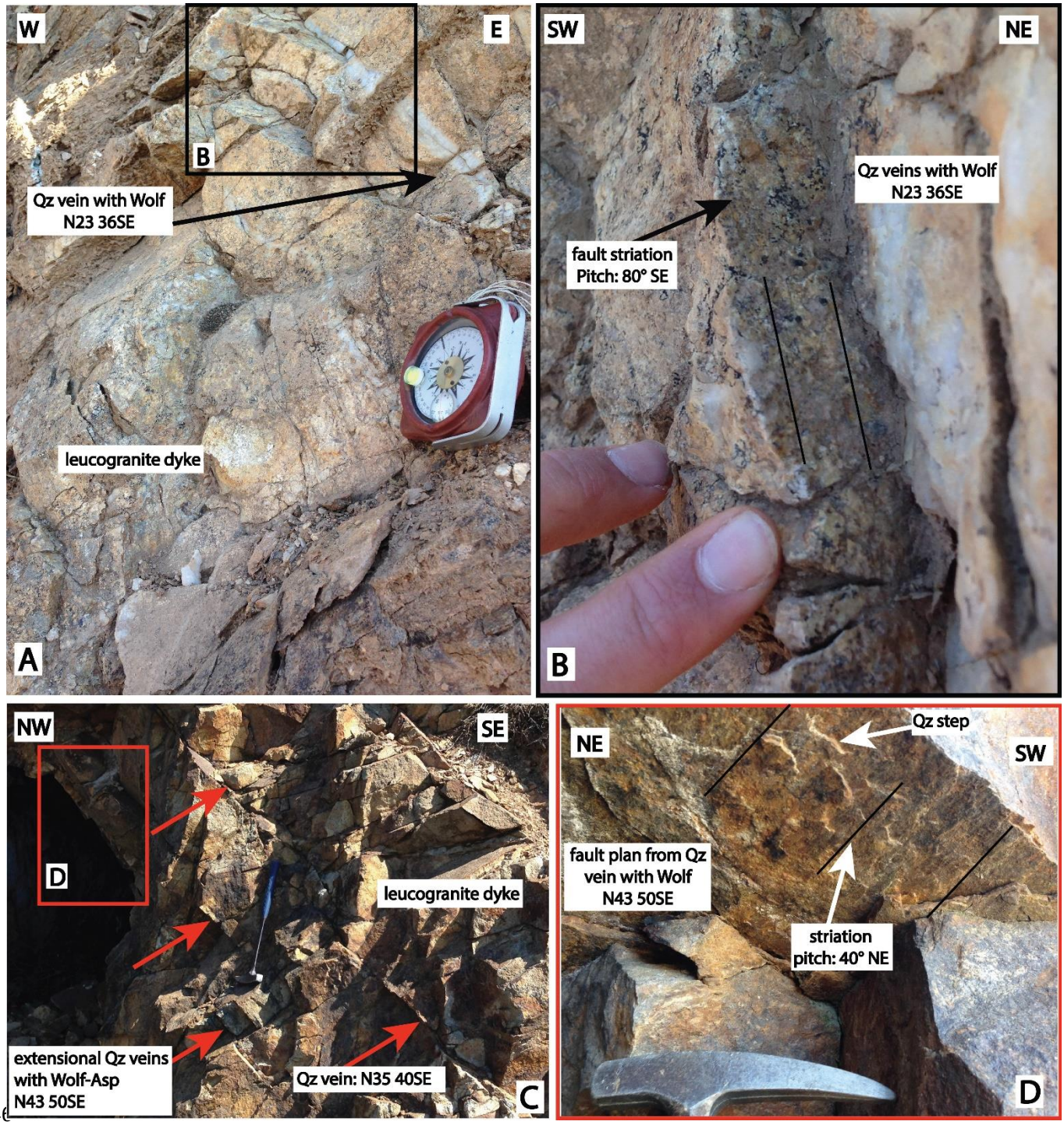
W
E
B
Qz vein with Wolf
N23 36SE
leucogranite dyke
A
SW
NE
Qz veins with Wolf
N23 36SE
fault striation
Pitch: 80° SE
B
NW
SE
D
leucogranite dyke
extensional Qz veins
with Wolf-Asp
N43 50SE
Qz vein: N35 40SE
C
NE
Qz step
SW
fault plan from Qz
vein with Wolf
N43 50SE
striation
pitch: 40° NE
D

Figure 6

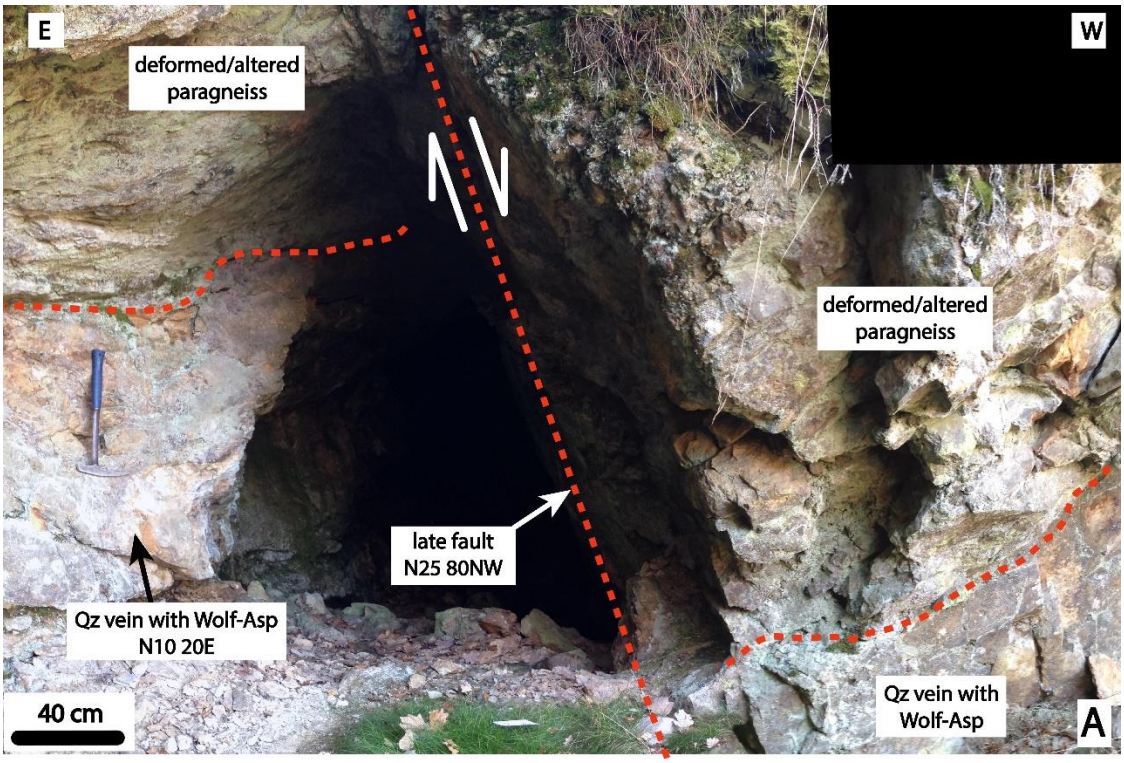
E
W
deformed/altered paragneiss
deformed/altered paragneiss
late fault N25 80NW
Qz vein with Wolf-Asp N10 20E
40 cm
Qz vein with Wolf-Asp
A

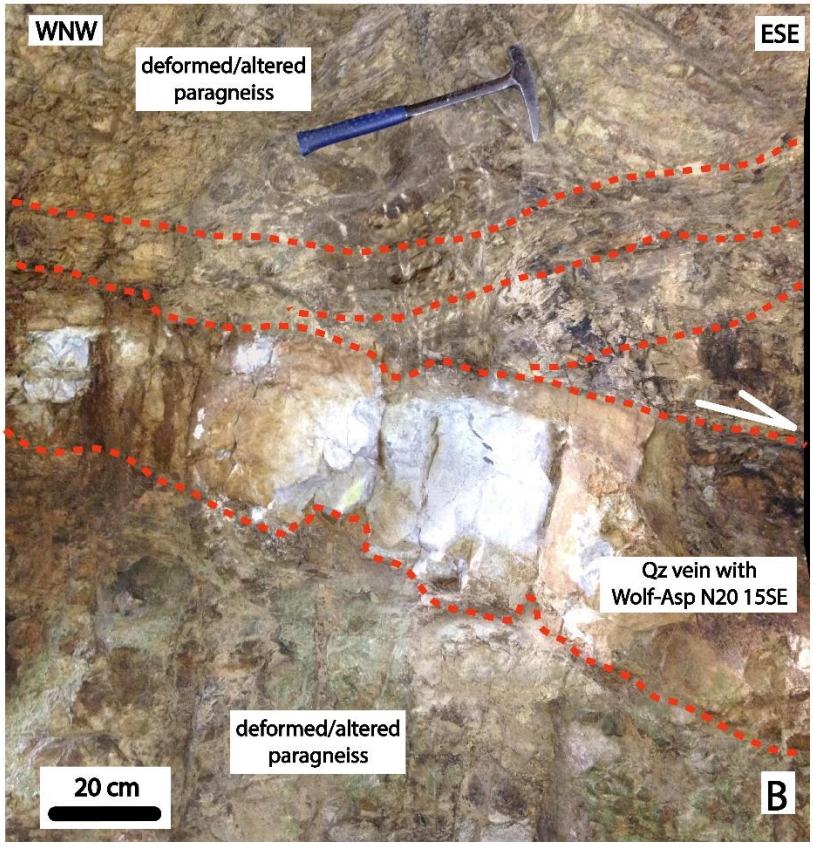
WNW
ESE
deformed/altered paragneiss
Qz vein with Wolf-Asp N20 15SE
deformed/altered paragneiss
20 cm
B

Figure 7

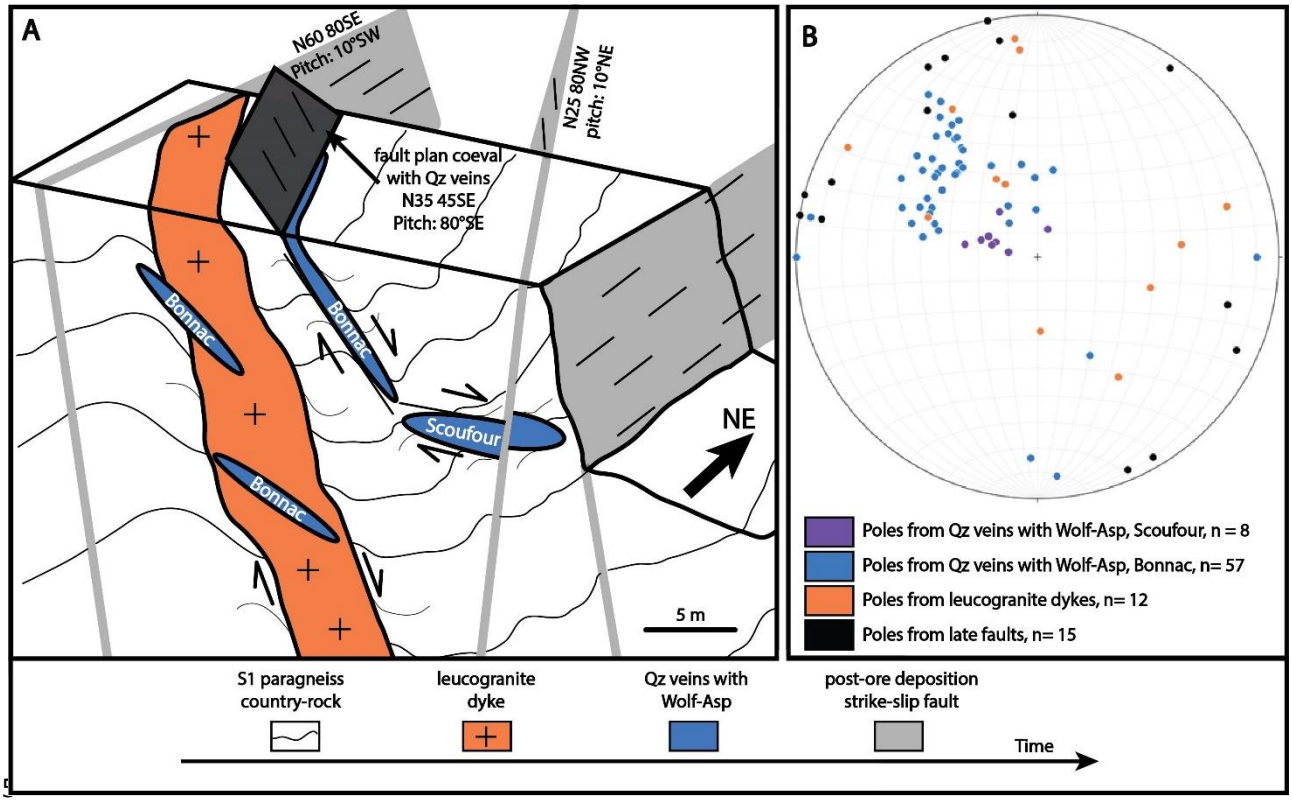

Figure 8

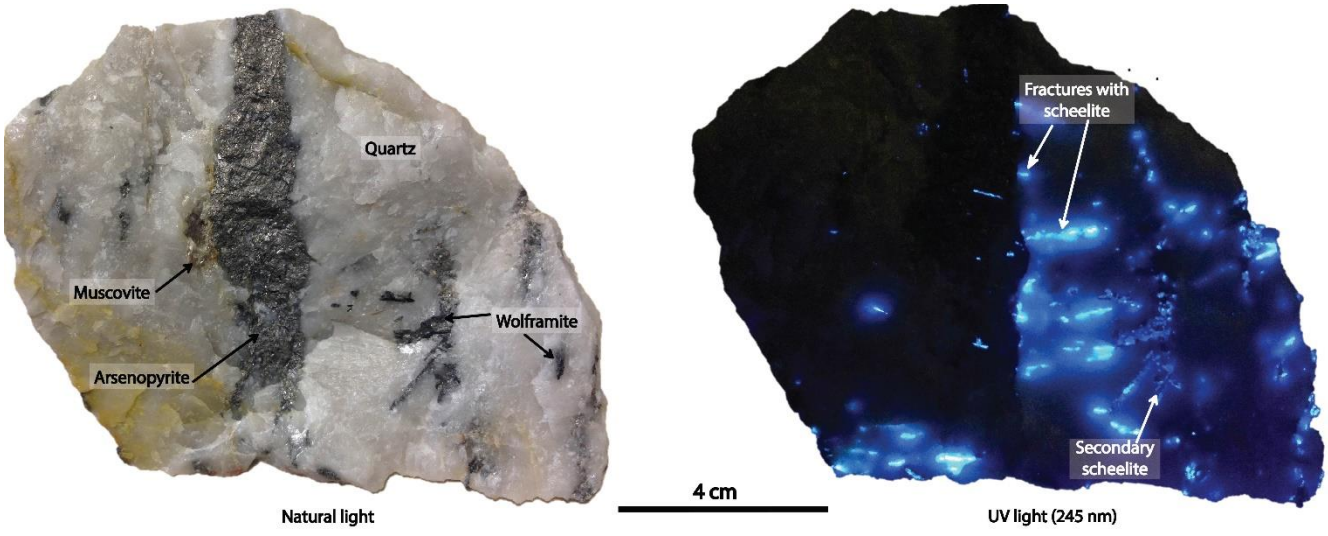

Figure 9

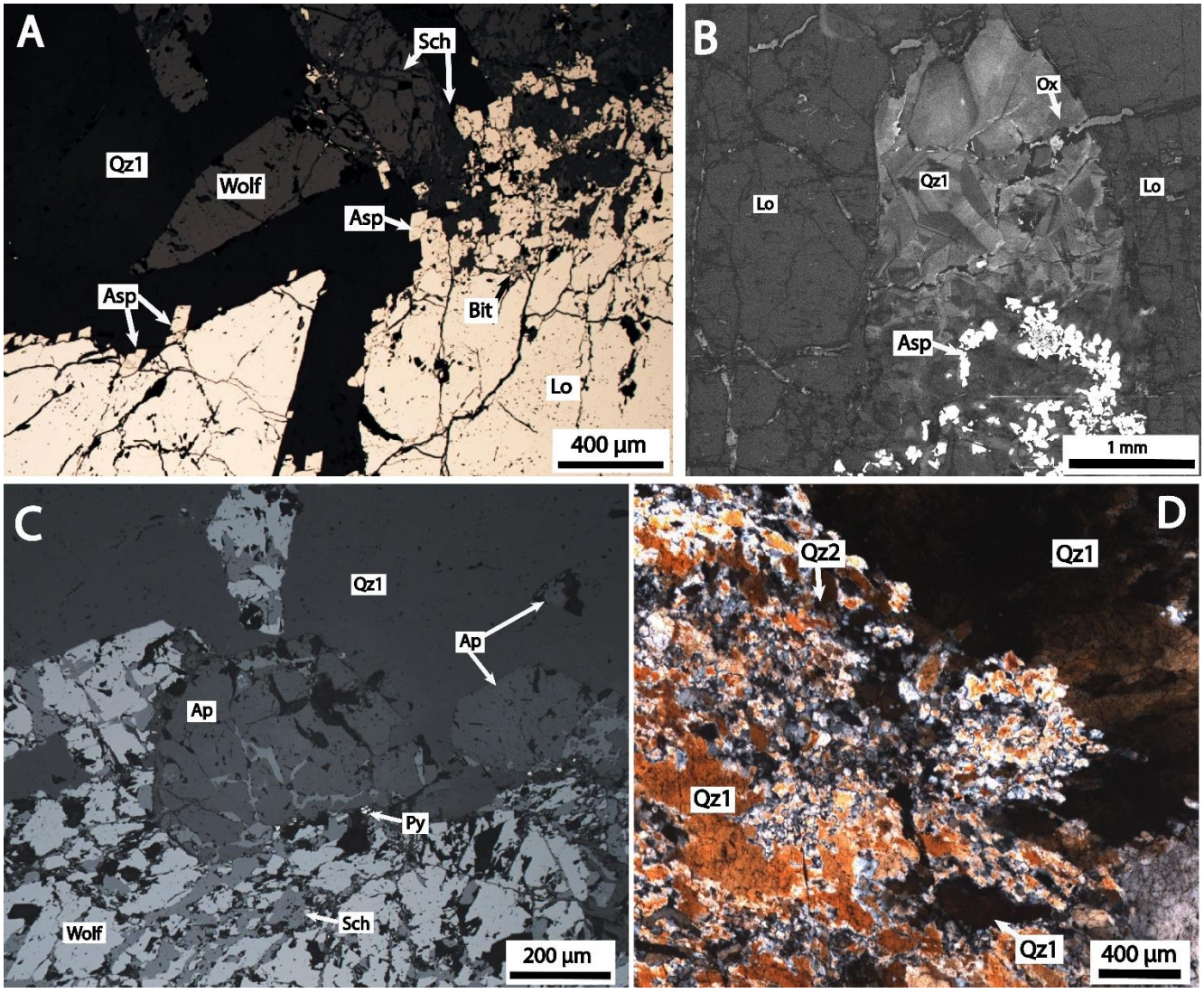
A
Sch
Qz1
Wolf
Asp
Asp
Bit
Lo
400 µm
B
Ox
Qz1
Lo
Lo
Asp
1 mm
C
Qz1
Ap
Ap
Py
Wolf
Sch
200 µm
D
Qz2
Qz1
Qz1
Qz1
400 µm

Figure 10

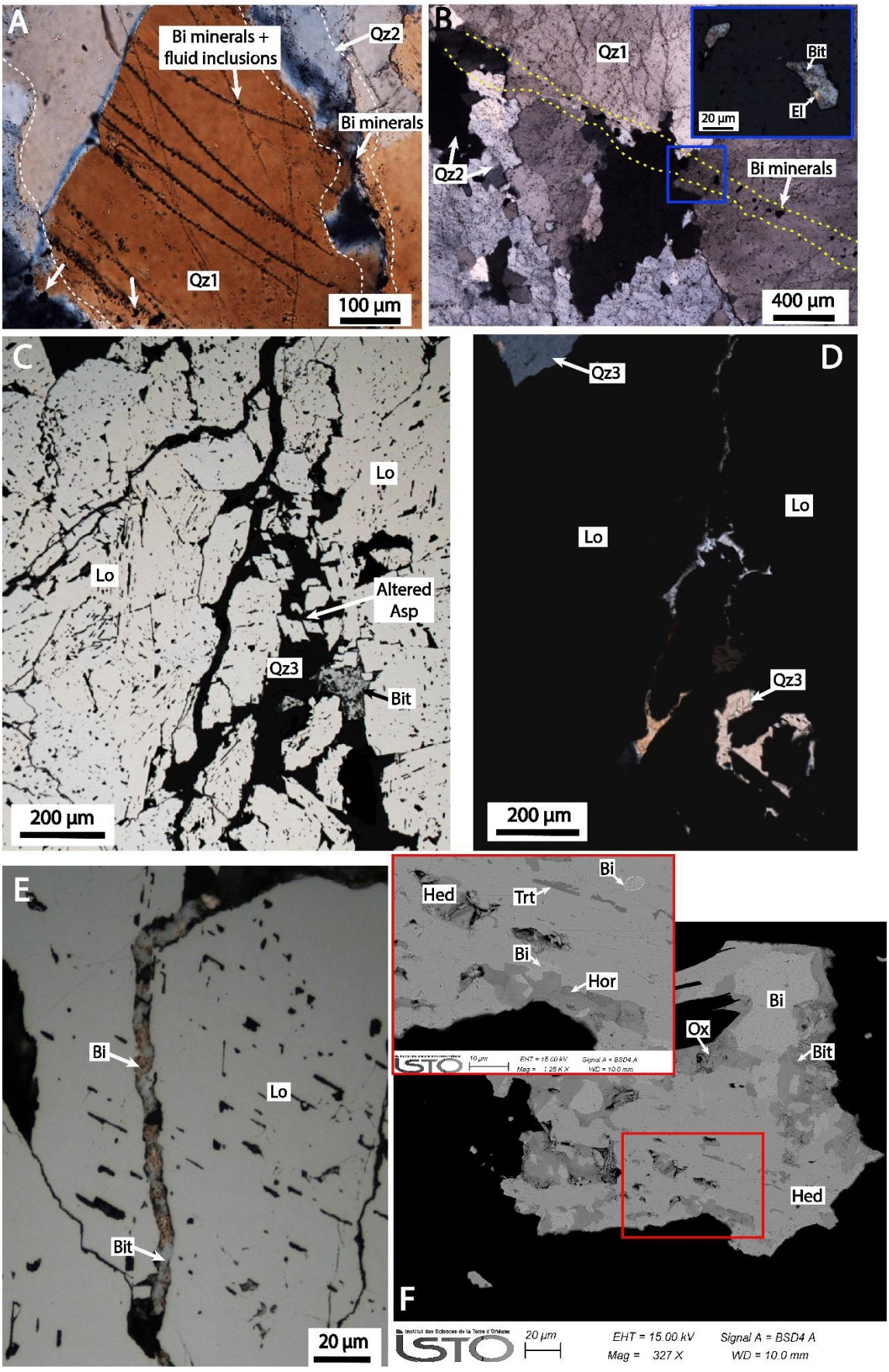
A
Bi minerals + fluid inclusions
Qz2
Bi minerals
Qz1
100 µm
B
Qz1
Bit
El
20 µm
Qz2
Bi minerals
400 µm
C
Lo
Lo
Altered Asp
Qz3
Bit
200 µm
D
Qz3
Lo
Lo
Qz3
200 µm
E
Bi
Lo
Bit
20 µm
Bi
Hed
Trt
Bi
Hor
Bi
Ox
Bit
Hed
F
20 µm
EHT = 15.00 kV
Mag = 327 X
Signal A = BSD4 A
WD = 10.0 mm

Figure 11

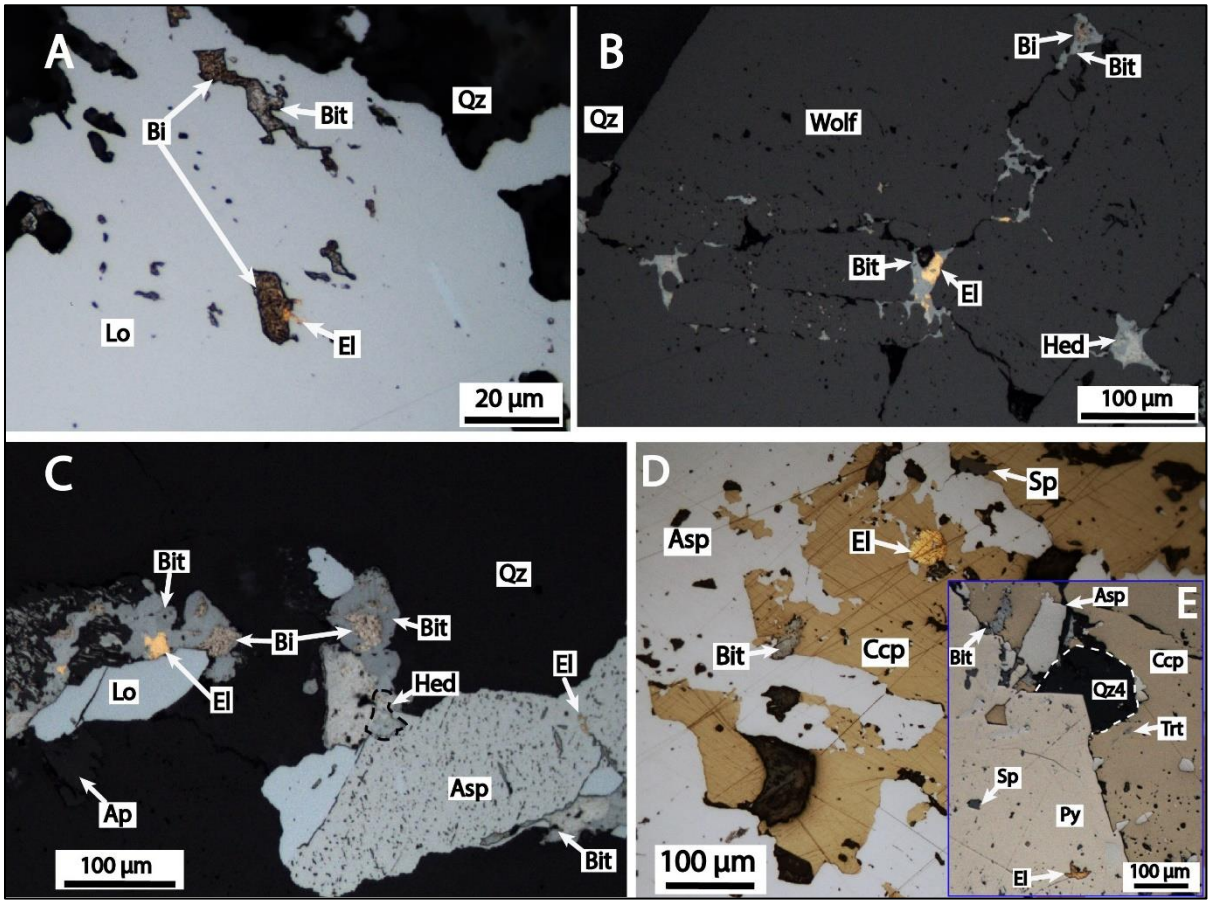
A
Bi
Bit
Qz
Lo
El
20 µm
B
Qz
Wolf
Bi
Bit
Bit
El
Hed
100 µm
C
Bit
Qz
Bi
Bit
Lo
El
Hed
El
Asp
Ap
100 µm
Bit
D
Sp
Asp
El
Bit
Ccp
100 µm
E
Asp
Bit
Ccp
Qz4
Trt
Sp
Py
El
100 µm

Figure 12

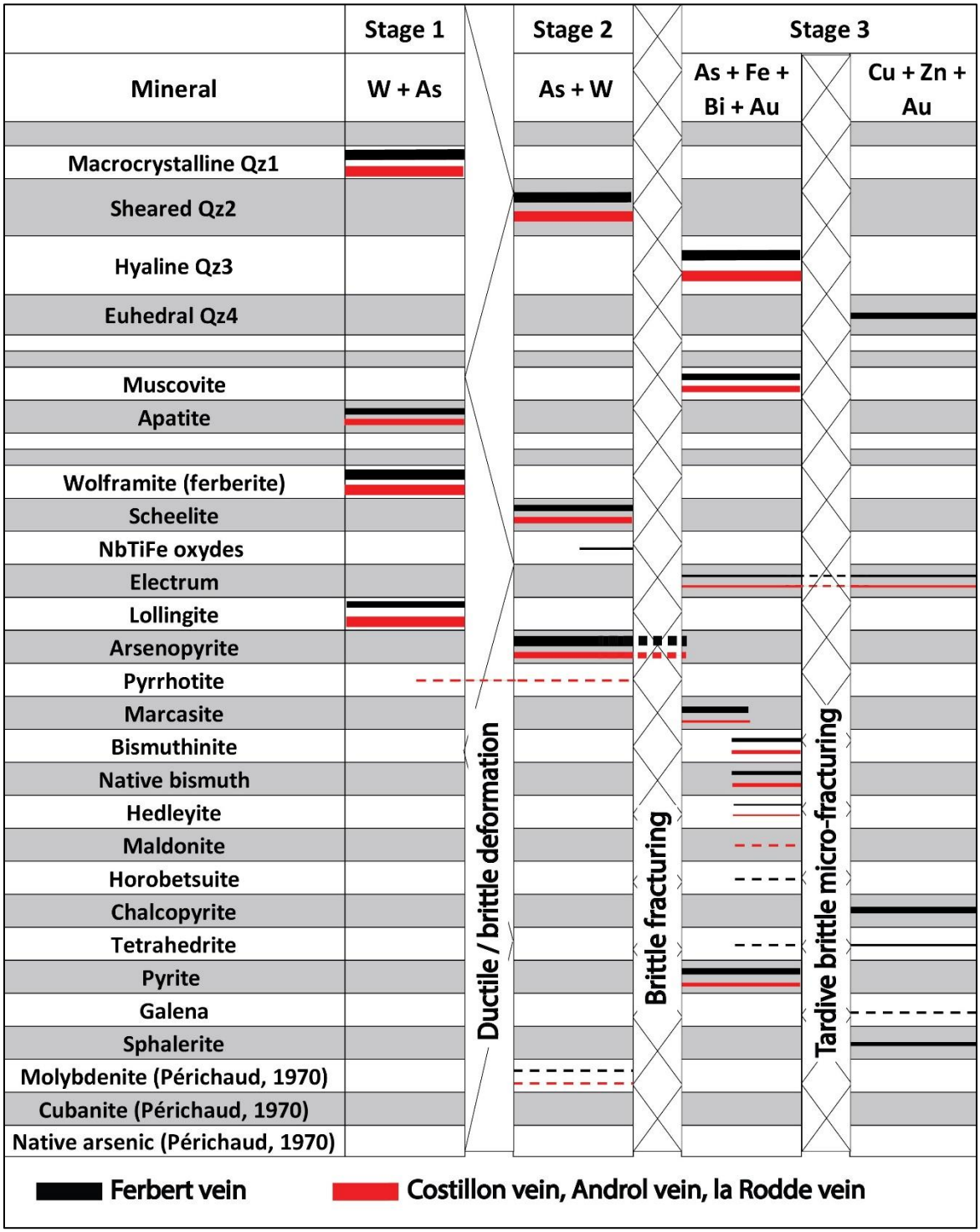
Stage 1
Stage 2
Stage 3
Mineral
W + As
As + W
As + Fe + Bi + Au
Cu + Zn + Au
Macrocrystalline Qz1
Sheared Qz2
Hyaline Qz3
Euhedral Qz4
Muscovite
Apatite
Wolframite (ferberite)
Scheelite
NbTiFe oxydes
Electrum
Lollingite
Arsenopyrite
Pyrrhotite
Marcasite
Bismuthinite
Native bismuth
Hedleyite
Maldonite
Horobetsuite
Chalcopyrite
Tetrahedrite
Pyrite
Galena
Sphalerite
Molybdenite (Périchaud, 1970)
Cubanite (Périchaud, 1970)
Native arsenic (Périchaud, 1970)
Ductile / brittle deformation
Brittle fracturing
Tardive brittle micro-fracturing
Ferbert vein
Costillon vein, Androl vein, la Rodde vein

Figure 13

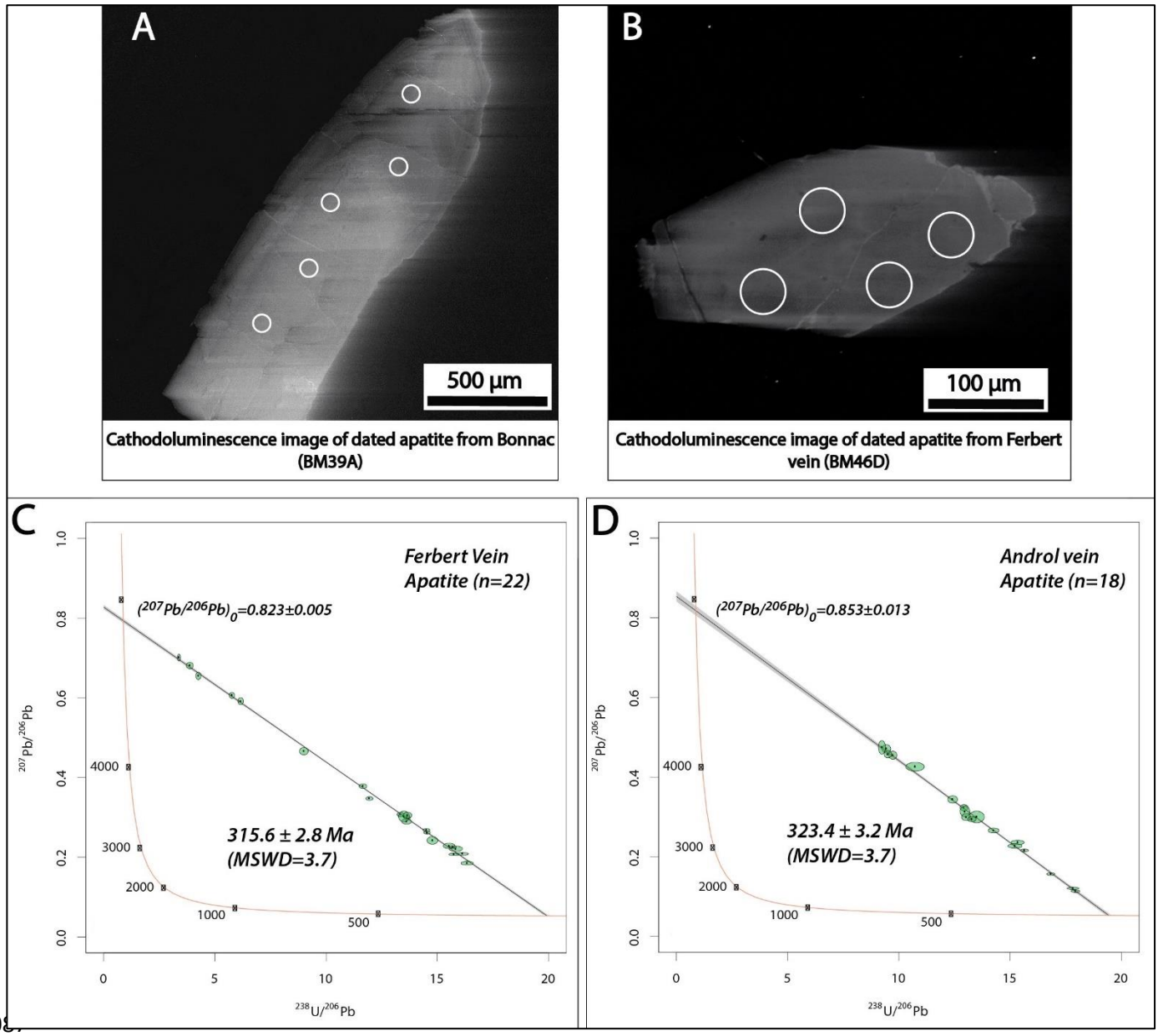
A
500 µm
Cathodoluminescence image of dated apatite from Bonnac (BM39A)
B
100 µm
Cathodoluminescence image of dated apatite from Ferbert vein (BM46D)
C
Ferbert Vein
Apatite (n=22)
(207Pb/206Pb)0=0.823±0.005
315.6 ± 2.8 Ma
(MSWD=3.7)
4000
3000
2000
1000
500
207Pb/206Pb
238U/206Pb
D
Androl vein
Apatite (n=18)
(207Pb/206Pb)0=0.853±0.013
323.4 ± 3.2 Ma
(MSWD=3.7)

Figure 14

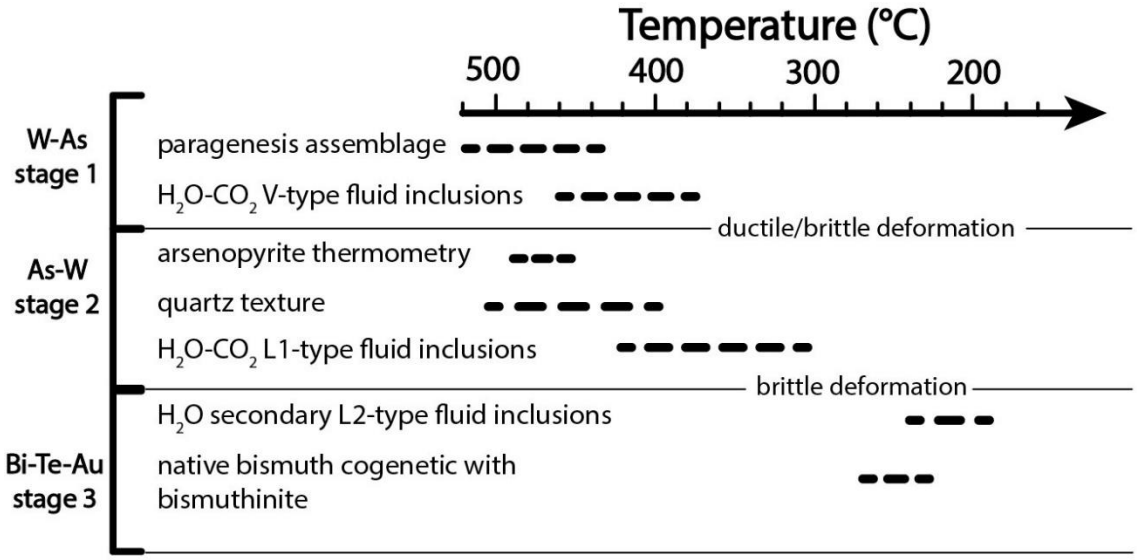

Figure 15

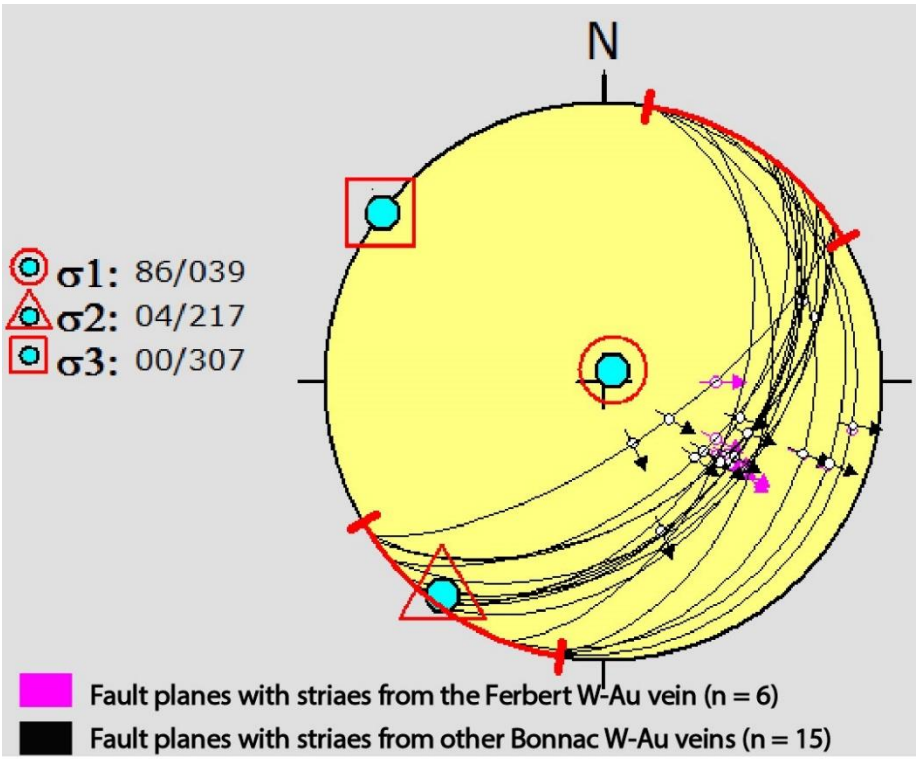

Figure 16

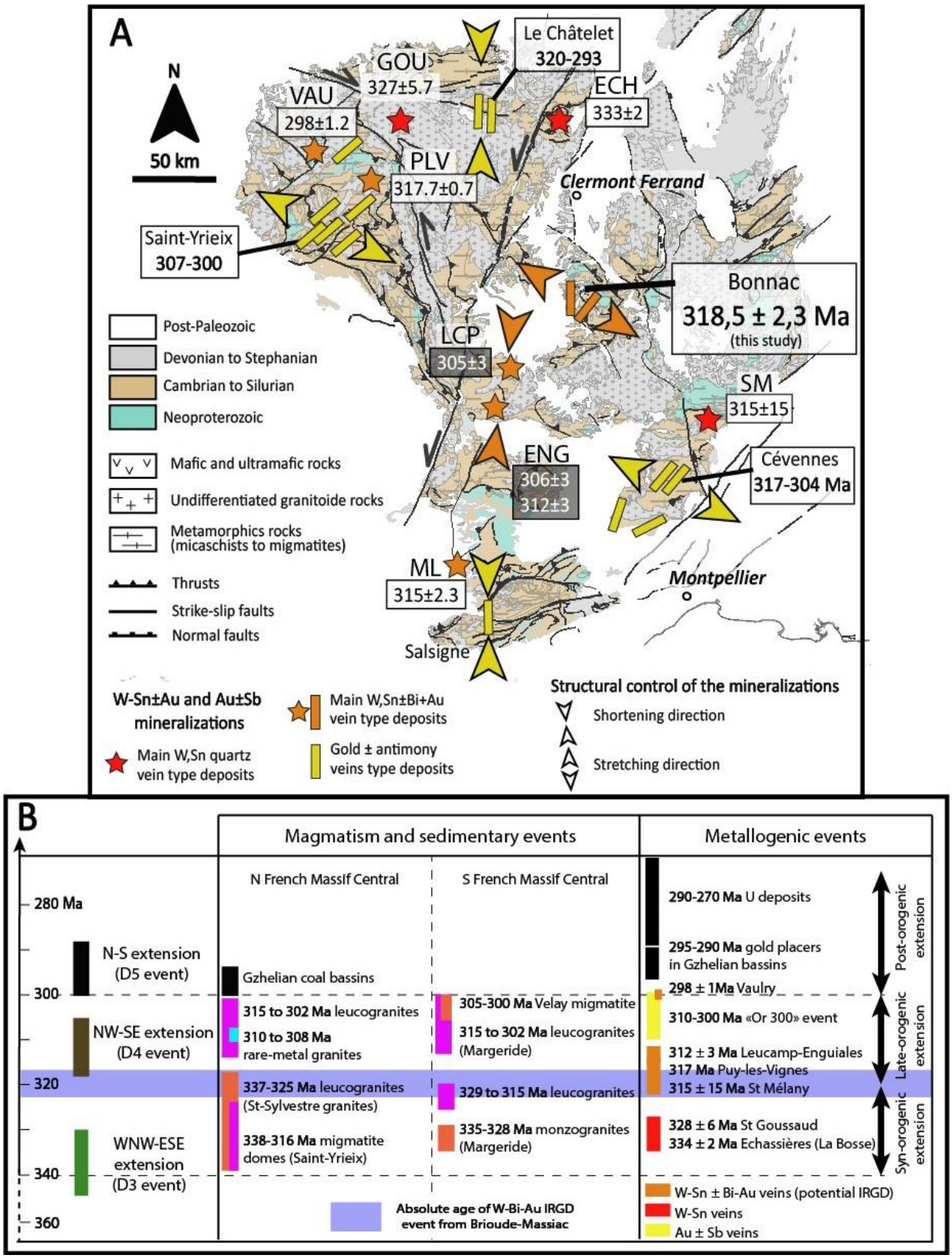
A
N
50 km
Le Châtelet
320-293
GOU
327±5.7
VAU
298±1.2
ECH
333±2
PLV
317.7±0.7
Clermont Ferrand
Saint-Yrieix
307-300
Bonnac
318,5 ± 2,3 Ma
(this study)
LCP
305±3
SM
315±15
ENG
306±3
312±3
Cévennes
317-304 Ma
ML
315±2.3
Montpellier
Salsigne
Post-Paleozoic
Devonian to Stephanian
Cambrian to Silurian
Neoproterozoic
Mafic and ultramafic rocks
Undifferentiated granitoide rocks
Metamorphics rocks
(micaschists to migmatites)
Thrusts
Strike-slip faults
Normal faults
W-Sn±Au and Au±Sb
mineralizations
Main W,Sn quartz
vein type deposits
Main W,Sn±Bi+Au
vein type deposits
Gold ± antimony
veins type deposits
Structural control of the mineralizations
Shortening direction
Stretching direction
B
Magmatism and sedimentary events
Metallogenic events
N French Massif Central
S French Massif Central
280 Ma
300
320
340
360
N-S extension
(D5 event)
NW-SE extension
(D4 event)
WNW-ESE
extension
(D3 event)
Gzhelian coal bassins
315 to 302 Ma leucogranites
310 to 308 Ma
rare-metal granites
337-325 Ma leucogranites
(St-Sylvestre granites)
338-316 Ma migmatite
domes (Saint-Yrieix)
305-300 Ma Velay migmatite
315 to 302 Ma leucogranites
(Margeride)
329 to 315 Ma leucogranites
335-328 Ma monzogranites
(Margeride)
Absolute age of W-Bi-Au IRGD
event from Brioude-Massiac
290-270 Ma U deposits
295-290 Ma gold placers
in Gzhelian bassins
298 ± 1Ma Vaulry
310-300 Ma «Or 300» event
312 ± 3 Ma Leucamp-Enguiales
317 Ma Puy-les-Vignes
315 ± 15 Ma St Mélany
328 ± 6 Ma St Goussaud
334 ± 2 Ma Echassières (La Bosse)
Post-orogenic extension
Late-orogenic extension
Syn-orogenic extension
W-Sn ± Bi-Au veins (potential IRGD)
W-Sn veins
Au ± Sb veins

Figure 17

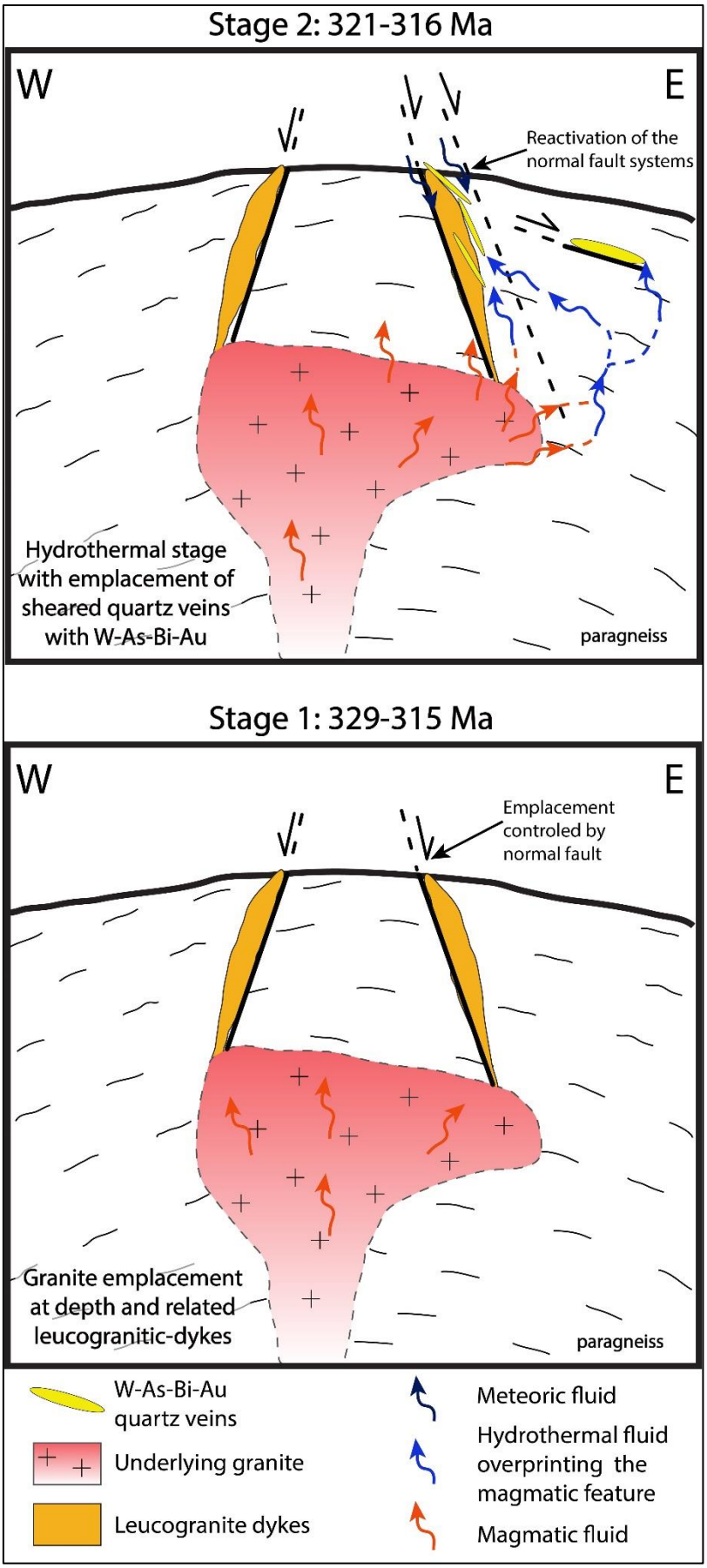
Stage 2: 321-316 Ma
W
E
Reactivation of the normal fault systems
Hydrothermal stage with emplacement of sheared quartz veins with W-As-Bi-Au
paragneiss
Stage 1: 329-315 Ma
W
E
Emplacement controled by normal fault
Granite emplacement at depth and related leucogranitic-dykes
paragneiss
W-As-Bi-Au quartz veins
Underlying granite
Leucogranite dykes
Meteoric fluid
Hydrothermal fluid overprinting the magmatic feature
Magmatic fluid

1099

Figure 18

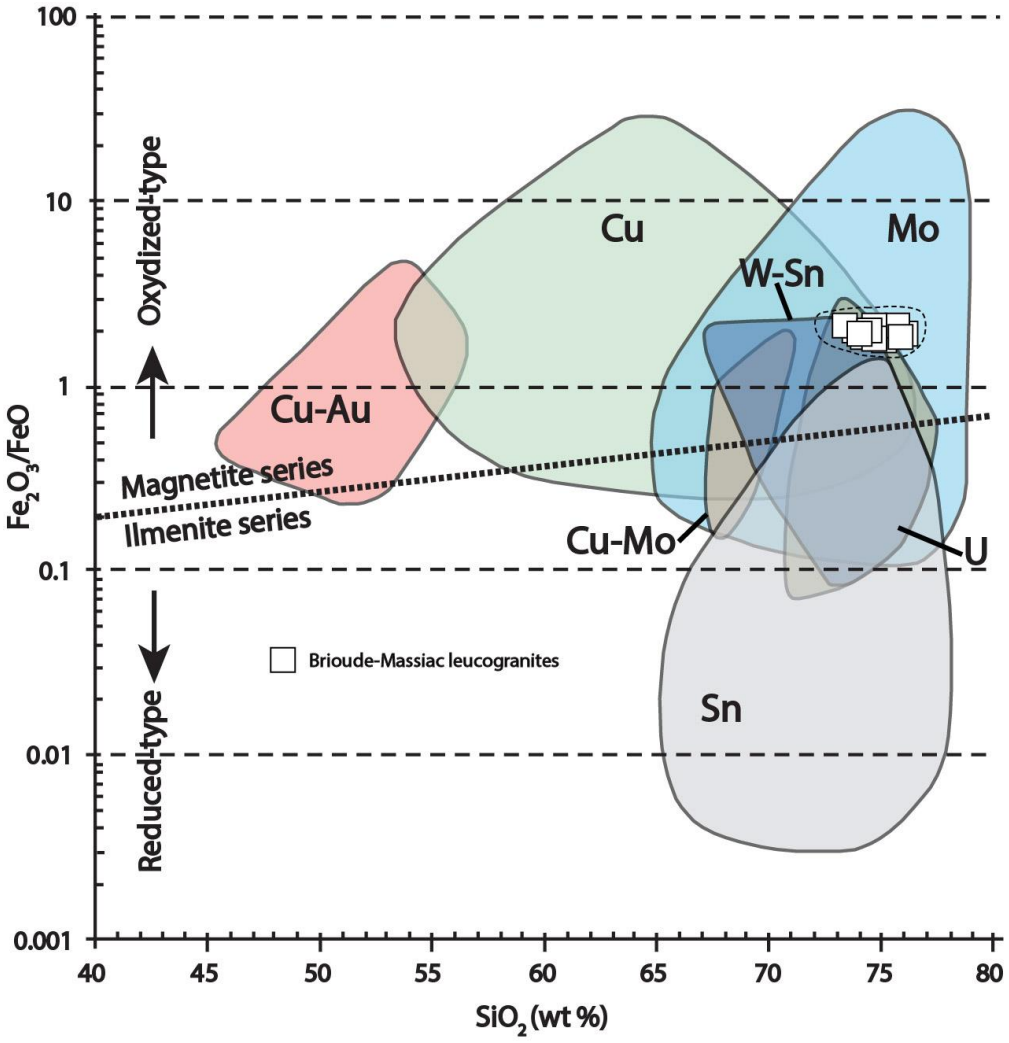
100
10
1
0.1
0.01
0.001
Oxydized-type
Reduced-type
Fe2O3/FeO
Cu
Mo
W-Sn
Cu-Au
Magnetite series
Ilmenite series
Cu-Mo
U
Brioude-Massiac leucogranites
Sn
40
45
50
55
60
65
70
75
80
SiO2 (wt %)

Table 1

Arsenopyrite composition	Number of analysis	S (Wt. %)	Std	Fe	Std	As	Std	Sb	Std	Au	Std	Total	As (at%)	Std	T (°C) Kretschmar and Scott, 1976	Trapping temperature (°C) estimated by fluid inclusions (Bril, 1982)
Asp from Bonnac W-As-Bi-Au veins (data from this study and Bril, 1983)	60	19.30	0.50	34.40	0.32	45.70	0.68	0.01	0.03	bdl		99.4	33.4	0.66	**485°C**	**> 350°C**
Asp from Vèze W-As-Bi-Au veins (data from Bril, 1983)	3	19.74	0.63	34.87	0.26	45.39	0.89	bdl		bdl		100	32.8	0.87	**470°C**	**> 350°C**
Asp from Bosberty W-As-Bi-Au veins (data from Bril, 1983)	4	19.10	0.46	35.43	0.19	45.47	0.63	bdl		bdl		100	33.0	0.61	**480°C**	**> 350°C**

Gold composition	Number of analysis	Ag (Wt. %)	Std	Au	Std	Total
Gold from W-As-Bi-Au veins	10	16.7	5.70	82.60	6.92	99.30

Std = standard dev bdl = below detection limit

Supplementary data

ESM 1

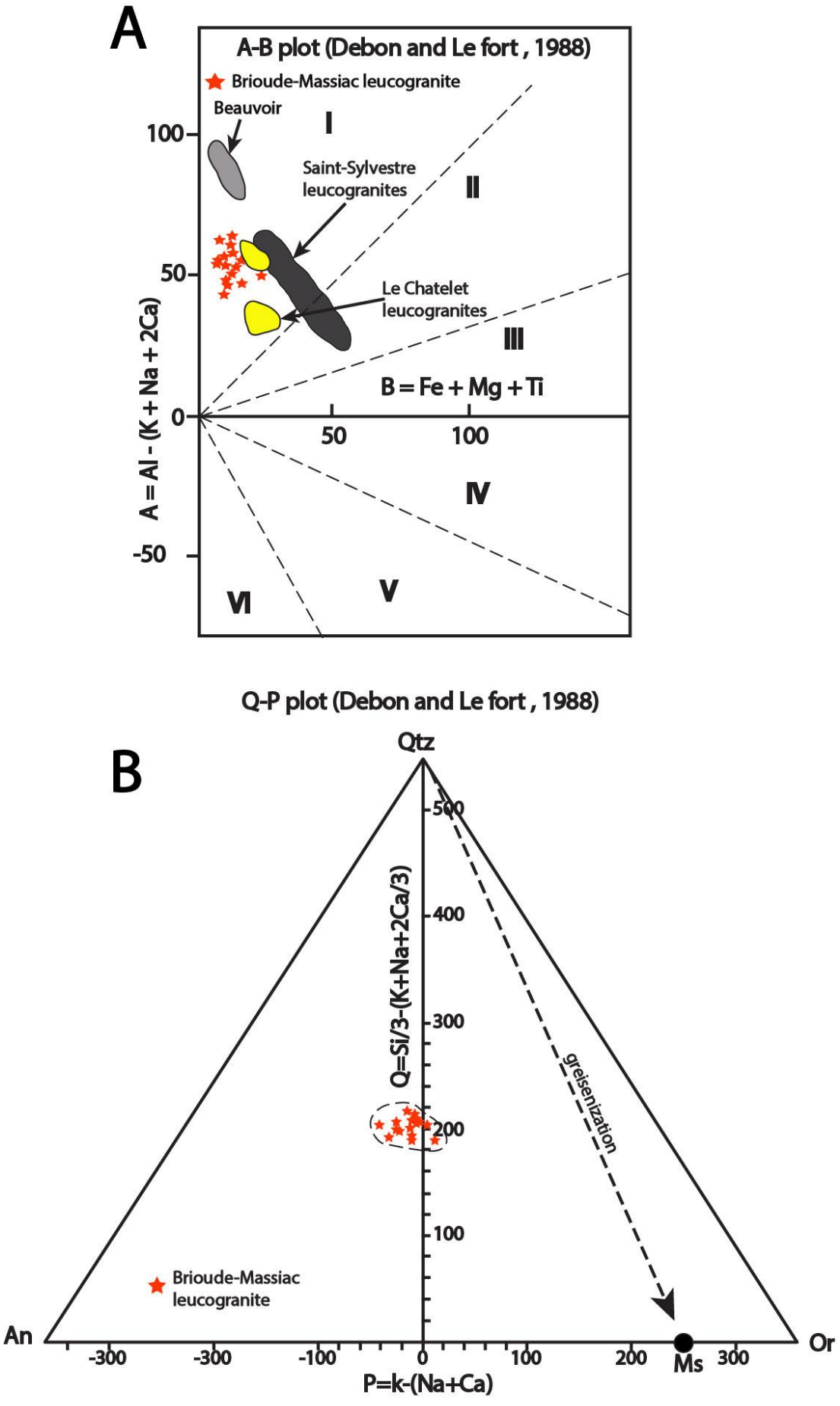
A
A-B plot (Debon and Le fort , 1988)
Brioude-Massiac leucogranite
Beauvoir
Saint-Sylvestre leucogranites
Le Chatelet leucogranites
I
II
III
IV
V
VI
100
50
0
-50
50
100
A = Al - (K + Na + 2Ca)
B = Fe + Mg + Ti
B
Q-P plot (Debon and Le fort , 1988)
Qtz
An
Or
Ms
500
400
300
200
100
-300
-300
-100
0
100
200
300
Q=Si/3-(K+Na+2Ca/3)
P=k-(Na+Ca)
greisenization
Brioude-Massiac leucogranite

1127 # ESM 2

Arsénopyrites

		Weight%						Det.Lim ppm					Atomic%					
Localisation	Commentaires	S	Sb	Fe	As	Au	Total	S	Sb	Fe	As	Au	S	Sb	Fe	As	Au	Total
Bonnac	BM29A_Asp1_coeur2	18.85	bdl	34.45	45.92	bdl	99.22	336	592	317	881	953	32.34	0.00	33.93	33.72	0.00	100
Bonnac	BM29A_Asp2_coeur	18.92	0.09	34.23	46.14	bdl	99.38	367	606	316	876	-	32.43	0.04	33.68	33.84	0.00	100
Bonnac	BM29A_Asp2_bord	18.65	bdl	34.19	46.79	bdl	99.63	364	596	311	885	-	31.99	0.00	33.67	34.34	0.00	100
Bonnac	BM29A_Asp3_C	19.00	0.09	34.58	46.44	bdl	100.11	390	605	323	882	-	32.34	0.04	33.79	33.83	0.00	100
Bonnac	BM29A_Asp3_B	19.38	bdl	34.62	45.88	bdl	99.87	363	-	311	876	-	32.91	0.00	33.75	33.34	0.00	100
Bonnac	BM29A_Asp4_C	19.19	bdl	34.13	45.96	bdl	99.27	389	599	318	880	-	32.83	0.00	33.52	33.65	0.00	100
Bonnac	BM29A_Asp5_B	19.17	bdl	34.27	46.36	bdl	99.79	374	602	317	882	-	32.67	0.00	33.52	33.81	0.00	100
Bonnac	BM29A_Asp5_C	18.96	bdl	34.25	46.38	bdl	99.59	364	596	314	881	-	32.43	0.00	33.63	33.94	0.00	100
Bonnac	BM29A_Asp6_C	19.14	bdl	34.66	46.16	bdl	99.96	380	597	313	887	-	32.55	0.00	33.85	33.60	0.00	100
Bonnac	BM29A_Asp6_C2	19.39	bdl	34.85	45.99	bdl	100.22	367	596	316	868	-	32.82	0.00	33.87	33.31	0.00	100
Bonnac	BM29A_Asp7_C	19.27	bdl	34.61	45.69	bdl	99.56	351	591	321	891	959	32.83	0.00	33.85	33.31	0.00	100
Bonnac	BM29A_Asp8_C	18.85	0.11	34.31	45.94	bdl	99.22	362	593	319	880	-	32.37	0.05	33.82	33.76	0.00	100
Bonnac	BM29A_Asp9_C	19.30	bdl	34.49	45.70	bdl	99.49	363	-	323	872	-	32.91	0.00	33.75	33.34	0.00	100
Bonnac	BM29A_Asp10_C	19.05	bdl	34.44	45.65	bdl	99.14	344	595	319	885	-	32.65	0.00	33.88	33.47	0.00	100
Bonnac	BM29A_Asp11_C	19.22	bdl	34.32	45.96	bdl	99.50	359	588	320	879	964	32.81	0.00	33.62	33.57	0.00	100
Bonnac	BM29A_Asp12_C	19.30	bdl	34.54	45.78	bdl	99.62	338	577	317	886	959	32.87	0.00	33.77	33.36	0.00	100
Bonnac	BM29A_Asp13_C	19.48	bdl	34.61	45.63	bdl	99.72	317	598	321	884	-	33.09	0.00	33.74	33.17	0.00	100
Bonnac	BM29A_Asp13_B	18.86	bdl	34.04	46.29	bdl	99.19	388	583	321	874	-	32.40	0.00	33.57	34.03	0.00	100
Bonnac	BM29A_Asp13_B2	20.10	bdl	34.49	44.91	bdl	99.49	396	597	317	867	-	34.00	0.00	33.49	32.51	0.00	100
Bonnac	BM29A_Asp14_C	19.41	bdl	34.42	45.69	bdl	99.52	372	597	314	872	-	33.06	0.00	33.64	33.30	0.00	100
Bonnac	BM29A_Asp15_B	19.16	bdl	34.34	46.29	bdl	99.79	389	602	317	874	-	32.64	0.00	33.60	33.76	0.00	100
Bonnac	BM29A_Asp16_C	18.88	bdl	34.26	46.28	bdl	99.42	359	584	320	875	-	32.35	0.00	33.71	33.94	0.00	100
Bonnac	BM29A_Asp16_B	19.00	bdl	33.37	45.21	bdl	97.59	347	588	314	883	-	33.05	0.00	33.31	33.64	0.00	100
Bonnac	BM29A_Asp17_C	19.02	bdl	34.27	46.04	bdl	99.32	358	-	314	880	-	32.57	0.00	33.69	33.74	0.00	100
Bonnac	BM29A_Asp18_C	19.28	bdl	34.56	45.91	bdl	99.75	366	594	322	875	956	32.80	0.00	33.77	33.43	0.00	100
Bonnac	BM29A_Asp18_B	19.99	bdl	34.37	44.25	bdl	98.61	379	586	314	868	-	34.08	0.00	33.64	32.28	0.00	100
Bonnac	BM29A_Asp19_C	19.57	bdl	34.55	45.19	0.13	99.44	364	585	319	876	959	33.30	0.00	33.75	32.91	0.04	100
Bonnac	BM29A_Asp20_C	19.24	bdl	34.19	45.78	bdl	99.21	379	585	318	869	-	32.92	0.00	33.57	33.51	0.00	100
Bonnac	BM29A_Asp21_C	19.21	bdl	34.37	45.94	bdl	99.51	380	-	311	881	-	32.79	0.00	33.67	33.55	0.00	100
Bonnac	BM29A_Asp22_C	19.84	bdl	34.47	44.46	bdl	98.76	376	584	316	861	-	33.83	0.00	33.74	32.44	0.00	100
Bonnac	BM29A_Asp23_C	19.24	bdl	34.36	45.80	bdl	99.40	388	597	314	870	-	32.85	0.00	33.68	33.47	0.00	100
Bonnac	BM29A_Asp23_B	19.89	bdl	34.32	45.19	bdl	99.40	397	-	311	875	957	33.76	0.00	33.43	32.81	0.00	100
Bonnac	BM29A_Asp24_B	19.11	bdl	34.34	46.04	bdl	99.48	388	-	322	879	958	32.65	0.00	33.68	33.67	0.00	100
Bonnac	BM29A_Asp25_C	19.28	0.15	34.39	45.88	bdl	99.69	367	600	316	870	-	32.84	0.07	33.63	33.45	0.00	100
Bonnac	BM29A_Asp25_C2	19.43	bdl	34.58	45.80	bdl	99.80	389	579	317	870	-	33.00	0.00	33.71	33.29	0.00	100
Bonnac	BM29A_Asp25_B	19.54	bdl	34.63	45.59	bdl	99.75	369	576	318	873	-	33.16	0.00	33.74	33.11	0.00	100
Bonnac	BM29A_Asp26_C	19.04	bdl	34.42	46.08	bdl	99.54	374	603	318	875	959	32.53	0.00	33.77	33.70	0.00	100
Bonnac	BM29A_Asp27_C	19.47	0.11	34.47	45.52	bdl	99.56	365	592	319	880		33.13	0.05	33.67	33.15	0.00	100
Bonnac	BM29A_Asp28_C	19.82	bdl	34.54	45.34	bdl	99.70	355	608	318	880	956	33.56	0.00	33.58	32.86	0.00	100
Bonnac	BM29A_Asp28_B	19.17	bdl	34.59	46.09	bdl	99.84	393	-	315	873	-	32.63	0.00	33.80	33.57	0.00	100
Bonnac	BM29A_Asp29_C	18.71	bdl	34.09	46.69	bdl	99.50	367	579	314	876	-	32.12	0.00	33.59	34.29	0.00	100
Bonnac	BM29A_Asp_30C	19.21	bdl	34.34	45.66	bdl	99.21	352	-	322	858	-	32.86	0.00	33.72	33.42	0.00	100
Bonnac	BM29A_Asp_30B	19.88	bdl	34.57	44.95	bdl	99.40	359	-	316	868	-	33.71	0.00	33.66	32.63	0.00	100
Bonnac	BM29A_Asp_31C	19.28	bdl	34.23	45.54	0.15	99.19	361	594	314	867	952	32.99	0.00	33.63	33.34	0.04	100
Bonnac	BM29A_Asp_31B	19.16	bdl	34.19	45.48	bdl	98.83	364	583	322	871	963	32.89	0.00	33.70	33.41	0.00	100
Bonnac	BM29A_Asp_32C	19.12	bdl	34.48	46.36	bdl	99.96	363	592	316	873	-	32.55	0.00	33.69	33.76	0.00	100
Bonnac	BM29A_Asp_32B	19.88	bdl	34.45	45.10	bdl	99.43	373	579	316	875	-	33.72	0.00	33.55	32.74	0.00	100
Bonnac	BM29A_Asp_33C	19.23	bdl	34.27	45.47	bdl	98.98	361	-	321	887	970	32.95	0.00	33.71	33.34	0.00	100
Bonnac	BM29A_Asp_34C	19.02	bdl	34.16	46.26	bdl	99.44	407	-	319	880	950	32.56	0.00	33.56	33.88	0.00	100
Bonnac	BM29A_Asp_35C	19.11	bdl	34.62	46.17	bdl	99.90	366	-	321	879	959	32.54	0.00	33.83	33.63	0.00	100
Bonnac	BM29A_Asp_36C	19.21	bdl	34.48	45.83	bdl	99.52	334	-	322	863	959	32.77	0.00	33.77	33.46	0.00	100
Bonnac	BM29A_Asp_37C	20.11	bdl	34.49	44.74	bdl	99.34	377	-	313	870	955	34.05	0.00	33.53	32.42	0.00	100
Bonnac	BM29A_Asp_37B	18.84	bdl	34.01	46.40	bdl	99.24	378	595	322	877	-	32.36	0.00	33.53	34.11	0.00	100
Bonnac	BM29A_Asp_38B	18.85	bdl	34.06	46.43	bdl	99.34	380	593	316	871	-	32.35	0.00	33.55	34.10	0.00	100
Bonnac	BM29A_Asp_38C	19.43	bdl	34.40	45.52	bdl	99.34	367	597	304	883	-	33.12	0.00	33.67	33.21	0.00	100
Bonnac	BM29A_Asp_39C	18.52	bdl	34.04	46.76	bdl	99.32	363	593	316	883	-	31.89	0.00	33.65	34.45	0.00	100

Grains d'or

		Weight%					Det.Lim ppm			
Localisation	Commentaires	Ag	Au	Hg	Sb	Total	Ag	Au	Hg	Sb
Bonnac	Or dans Py/Ccp	16.07	84.57	bdl	bdl	100.64	696	2284	-	-
Bonnac	Or dans Py/Ccp	11.05	89.77	bdl	bdl	100.82	692	2307	-	-
Bonnac	Or dans Py/Ccp	8.81	92.37	bdl	bdl	101.18	584	1975	-	1190
Bonnac	Or dans Py/Ccp	7.85	91.86	bdl	bdl	99.71	552	1936	-	-
Bonnac	Or dans Py/Ccp	17.18	83.07	bdl	bdl	100.26	609	1971	-	1216
Bonnac	Or dans Py/Ccp	19.63	77.84	0.29	bdl	97.77	594	1985	1136	-
Bonnac	Or dans Py/Ccp	20.05	78.97	bdl	bdl	99.02	598	1967	1131	-
Bonnac	Or inclus dans Ccp+Bi	19.68	79.53	bdl	bdl	99.21	589	1977	-	1174
Bonnac	Or inclus dans Ccp+Bi	22.14	76.34	bdl	bdl	98.48	594	1968	-	1213
Bonnac	Or inclus dans Asp	24.51	72.12	0.42	bdl	97.04	613	1964	1121	1175

1128

ESM 3

ESM 3 Table 1: Operating conditions for the LA-ICP-MS equipment	
Laboratory & Sample Preparation	
Laboratory name	Géosciences Rennes, UMR CNRS 6118, Rennes, France
Sample type/mineral	apatite
Sample preparation	Thin and polished sections
Imaging	MEB Merlin Compact Zeiss with EDS detector EDS (Bruker, Quantax – Xflash6– 129 eV)
Laser ablation system	
Make, Model & type	ESI NWR193UC, Excimer
Ablation cell	ESI NWR TwoVol2
Laser wavelength	193 nm
Pulse width	< 5 ns
Fluence	6.5 J/cm^2
Repetition rate	5 Hz
Spot sizes	40 µm (round spot)
Sampling mode / pattern	Single spot
Carrier gas	100% He, Ar make-up gas and N2 (3 ml/mn) combined using in-house smoothing device
Background collection	20 seconds
Ablation duration	60 seconds
Wash-out delay	15 seconds
Cell carrier gas flow (He)	0.75 l/min
ICP-MS Instrument	
Make, Model & type	Agilent 7700x, Q-ICP-MS
Sample introduction	Via conventional tubing
RF power	1350W
Sampler, skimmer cones	Ni
Extraction lenses	X type
Make-up gas flow (Ar)	0.87 l/min
Detection system	Single collector secondary electron multiplier
Data acquisition protocol	Time-resolved analysis
Scanning mode	Peak hopping, one point per peak
Detector mode	Pulse counting, dead time correction applied, and analog mode when signal intensity > ~ 10^6 cps
Masses measured	^{43}Ca, ^{204}(Hg + Pb), ^{206}Pb, ^{207}Pb,^{208}Pb, ^{232}Th, ^{238}U
Integration time per peak	10-30 ms
Sensitivity / Efficiency	28 000 cps/ppm Pb (50µm, 10Hz)
Dwell time per isotope	5-70 ms depending on the masses
Data Processing	
Gas blank	20 s on-peak
Calibration strategy	Madagascar apatite used as primary reference material, Durango and McClure apatite standards
	used as secondary reference material (quality control)
Reference Material info	Madagascar (Thomson et al., 2012) Durango (McDowell et al., 2005) McClure (Schoene and Bowring, 2006)
Data processing package used	Iolite (Paton et al., 2010), VizualAge_UcomPbine (Chew et al., 2014)
Quality control / Validation	Durango: Weighted average ^{207}Pb corrected age = 31.89 ± 0.70 Ma (MSWD = 0.62)
	McClure: Weighted average ^{207}Pb corrected age = 526 ± 14 Ma (MSWD = 1.7)

	ESM 3 Table 2: LA-ICP-MS U/Pb analyses for apatites for studied samples								
		U (ppm)	Pb (ppm)	238U/206Pb	Error (2σ)	207Pb/206Pb	Error (2σ)	Final 207 Age	Error (2σ)
	BM46d_1	111.90	7.82	15.830	0.250	0.2212	0.0054	317	16
	BM46d_2	122.60	7.77	16.130	0.220	0.2083	0.0030	316	14
	BM46d_3	115.90	8.24	15.530	0.220	0.2283	0.0053	317	13
	BM46d_4	88.40	8.02	14.510	0.130	0.2680	0.0031	318	17
	BM46d_5	127.60	10.31	15.700	0.130	0.2254	0.0024	316	17
	BM46d_7	66.10	7.61	13.350	0.130	0.3069	0.0044	324	19
	BM46d_8	73.70	7.89	13.620	0.180	0.2896	0.0054	327	16
	BM46d_9	176.80	10.11	16.340	0.230	0.1849	0.0039	324	17
	BM46d_10	64.44	7.24	13.640	0.120	0.2992	0.0037	322	18
	BM46d_11	148.70	10.11	15.750	0.190	0.2071	0.0027	324	16
	BM46d_13	66.79	10.16	11.660	0.140	0.3781	0.0048	323	22
	BM46d_14	158.30	13.75	14.540	0.120	0.2616	0.0031	322	16
	BM46d_15	90.33	14.57	11.950	0.130	0.3472	0.0039	336	21
	BM46d_16	97.10	10.38	13.500	0.200	0.3023	0.0110	322	21
	BM46d_17	41.64	21.18	5.768	0.096	0.6060	0.0063	344	43
	BM46d_18	39.08	40.03	3.384	0.055	0.7010	0.0070	369	63
	BM46d_19	51.83	12.96	9.000	0.160	0.4660	0.0077	343	30
	BM46d_20	51.96	39.50	4.255	0.091	0.6550	0.0077	377	44
	BM46d_21	38.60	33.40	3.870	0.130	0.6810	0.0066	362	40
	BM46d_22	207.80	17.13	14.780	0.200	0.2421	0.0078	327	16
	BM46d_23	204.30	22.95	13.660	0.160	0.3051	0.0062	317	11
Ferbert vein	BM46d_24	68.00	32.18	6.160	0.100	0.5915	0.0075	341	20
Bonnac	BM39a_2	29.06	3.39	12.930	0.150	0.3233	0.0063	324	14
	BM39a_3	30.09	3.58	12.970	0.180	0.3140	0.0110	333	13
	BM39a_4	26.70	2.79	13.030	0.170	0.2997	0.0074	336	16
	BM39a_5	24.32	2.65	13.500	0.280	0.3000	0.0120	325	22
	BM39a_6	11.66	2.86	9.440	0.160	0.4710	0.0085	323	28
	BM39a_7	13.39	3.39	9.730	0.150	0.4550	0.0083	326	23
	BM39a_8	13.13	3.52	9.510	0.140	0.4573	0.0075	333	25
	BM39a_9	13.53	2.97	10.730	0.340	0.4260	0.0090	321	29
	BM39a_10	11.25	3.02	9.240	0.130	0.4747	0.0140	326	24
	BM39a_11	23.39	3.31	12.420	0.180	0.3438	0.0077	324	16
	BM39a_13	138.10	5.24	16.830	0.150	0.1567	0.0027	325	11
	BM39a_14	76.90	5.10	15.340	0.240	0.2360	0.0047	319	12
	BM39a_15	315.50	6.81	17.830	0.220	0.1208	0.0026	324	12
	BM39a_16	79.80	5.17	15.220	0.260	0.2271	0.0045	325	13
	BM39a_17	76.51	4.93	15.650	0.150	0.2160	0.0027	320	12
	BM39a_19	243.20	5.29	17.940	0.160	0.1138	0.0027	324	11
	BM39a_21	34.74	3.53	13.280	0.160	0.2944	0.0052	332	16
	BM39a_24	48.50	4.04	14.260	0.200	0.2660	0.0052	326	15